CANCER

The brain-penetrant clinical ATM inhibitor AZD1390 radiosensitizes and improves survival of preclinical brain tumor models

Stephen T. Durant[1]*†, Li Zheng[2]†‡, Yingchun Wang[2]‡, Kan Chen[3]‡, Lingli Zhang[3]‡, Tianwei Zhang[2]‡, Zhenfan Yang[2]‡, Lucy Riches[1], Antonio G. Trinidad[1], Jacqueline H. L. Fok[1], Tom Hunt[4], Kurt G. Pike[4], Joanne Wilson[5], Aaron Smith[5], Nicola Colclough[5], Venkatesh Pilla Reddy[5], Andrew Sykes[5], Annika Janefeldt[6], Peter Johnström[7], Katarina Varnäs[8], Akihiro Takano[8], Stephanie Ling[9], Jonathan Orme[9], Jonathan Stott[9], Caroline Roberts[9], Ian Barrett[9], Gemma Jones[10], Martine Roudier[10], Andrew Pierce[10], Jasmine Allen[11], Jenna Kahn[11], Amrita Sule[11], Jeremy Karlin[11], Anna Cronin[12], Melissa Chapman[12], Kristoffer Valerie[11], Ruth Illingworth[13], Martin Pass[14]

Poor survival rates of patients with tumors arising from or disseminating into the brain are attributed to an inability to excise all tumor tissue (if operable), a lack of blood-brain barrier (BBB) penetration of chemotherapies/targeted agents, and an intrinsic tumor radio-/chemo-resistance. Ataxia-telangiectasia mutated (ATM) protein orchestrates the cellular DNA damage response (DDR) to cytotoxic DNA double-strand breaks induced by ionizing radiation (IR). ATM genetic ablation or pharmacological inhibition results in tumor cell hypersensitivity to IR. We report the primary pharmacology of the clinical-grade, exquisitely potent (cell IC_{50}, 0.78 nM), highly selective [>10,000-fold over kinases within the same phosphatidylinositol 3-kinase–related kinase (PIKK) family], orally bioavailable ATM inhibitor AZD1390 specifically optimized for BBB penetration confirmed in cynomolgus monkey brain positron emission tomography (PET) imaging of microdosed ^{11}C-labeled AZD1390 ($K_{p,uu}$, 0.33). AZD1390 blocks ATM-dependent DDR pathway activity and combines with radiation to induce G_2 cell cycle phase accumulation, micronuclei, and apoptosis. AZD1390 radiosensitizes glioma and lung cancer cell lines, with p53 mutant glioma cells generally being more radiosensitized than wild type. In in vivo syngeneic and patient-derived glioma as well as orthotopic lung-brain metastatic models, AZD1390 dosed in combination with daily fractions of IR (whole-brain or stereotactic radiotherapy) significantly induced tumor regressions and increased animal survival compared to IR treatment alone. We established a pharmacokinetic-pharmacodynamic-efficacy relationship by correlating free brain concentrations, tumor phospho-ATM/phospho-Rad50 inhibition, apoptotic biomarker (cleaved caspase-3) induction, tumor regression, and survival. On the basis of the data presented here, AZD1390 is now in early clinical development for use as a radiosensitizer in central nervous system malignancies.

INTRODUCTION

Glioblastoma multiforme (GBM)—the most common and lethal form of brain tumor arising from malignant glial cells (astrocytes and oligodendrocytes)—affects 2 to 3 per 100,000 adults per year and accounts for 52% of all primary brain tumors (*1*). Despite survival benefits afforded to patients by current treatment, standard of care surgery followed by fractionated radiotherapy and temozolomide (TMZ), median survival remains just 12 to 15 months (*1*, *2*). Poor survival is attributed to an inability to excise all invasive tumor tissue (if operable), inadequate exposures of anticancer agents to tumors protected by the blood-brain barrier (BBB), and an intrinsic tumor radio- and chemoresistance. In addition to rarer adult and pediatric primary brain tumors (for example, medulloblastoma, choroid plexus carcinoma, ependymoma, and diffuse intrinsic pontine glioma) and an order of magnitude greater in occurrence than GBM are secondary brain tumors most commonly arising from metastatic non–small cell lung cancer, melanoma, and breast cancer. Brain metastases are also frequently refractory to current chemotherapy/radiotherapy regimes, and their occurrence usually signifies end-stage disease (*3*). Ataxia-telangiectasia mutated (ATM) serine/threonine protein kinase is a member of the phosphatidylinositol 3-kinase (PI3K)–related kinase (PIKK) family [also comprising ataxia telangiectasia and Rad3-related (ATR),

---

[1]Bioscience, Oncology Innovative Medicines and Early Development (IMED) Biotech Unit, AstraZeneca, Cambridge, UK. [2]Bioscience, Innovative Cancer Centre, Oncology IMED Biotech Unit, AstraZeneca, Shanghai, China. [3]Drug Metabolism and Pharmacokinetics, Innovative Cancer Centre, Oncology IMED Biotech Unit, AstraZeneca, Shanghai, China. [4]Chemistry, Oncology IMED Biotech Unit, AstraZeneca, Cambridge, UK. [5]Drug Metabolism and Pharmacokinetics, Oncology IMED Biotech Unit, AstraZeneca, Cambridge, UK. [6]Drug Metabolism and Pharmacokinetics, Cardiovascular and Metabolic Diseases IMED Biotech Unit, AstraZeneca, Gothenburg, Sweden. [7]Precision Medicine and Genomics, IMED Biotech Unit, AstraZeneca, Karolinska Institutet, Stockholm, Sweden. [8]Department of Clinical Neuroscience, Center for Psychiatry Research, Karolinska Institutet and Stockholm County Council, Stockholm, Sweden. [9]Discovery Sciences, Oncology IMED Biotech Unit, AstraZeneca, Cambridge, UK. [10]Translational Sciences, Oncology IMED Biotech Unit, AstraZeneca, Cambridge, UK. [11]Department of Radiation Oncology, Massey Cancer Center, Virginia Commonwealth University, Richmond, VA 23298–0058, USA. [12]Drug Safety and Metabolism, Oncology IMED Biotech Unit, AstraZeneca, Cambridge, UK. [13]Operations, AstraZeneca, Waltham, MA 02451, USA. [14]Projects, Oncology IMED Biotech Unit, AstraZeneca, Cambridge, UK.
*Corresponding author. Email: stephen.durant@astrazeneca.com

†These authors contributed equally to this work.

‡Present address: Dizal (Jiangsu) Pharmaceutical Co. Ltd., Shanghai, China.

DNA-dependent protein kinase, catalytic subunit (DNA-PKcs), mammalian target of rapamycin (mTOR), nonsense mediated mRNA decay associated PI3K related kinase (SMG1), and transformation/transcription domain-associated protein (TRRAP)] (*4*). ATM plays a central role in the detection, signaling, and repair of DNA double-strand breaks (DSBs), which are the most cytotoxic DNA lesion induced by ionizing radiation (IR) and certain chemotherapies. A-T (ataxia-telangiectasia) is an autosomal recessive disorder resulting from mutations in the *ATM* gene, and patients suffer a variety of symptoms including extreme radiosensitivity. Cells from A-T patients and knockout mice display abnormal cell cycle arrest in the G_1, S, and G_2 phases and extreme hypersensitivity to IR (*5*–*11*). ATM is recruited to sites of DSBs by the DNA end-tethering MRE11-RAD50-NBS1 complex and results in ATM activation by autophosphorylation at Ser^{1981} (*12*). This leads to a rapid amplified phosphorylation of nearby chromatin on Ser^{139} of histone variant H2AX (γH2AX), which initiates the assembly of DNA damage response (DDR) components at the breakage site to facilitate DNA DSB repair—by either homologous recombination (HR) or nonhomologous end-joining (NHEJ) depending on the availability of homologous chromosomal sequences at various stages of the cell cycle (*13*–*15*). ATM activation also signals cell cycle arrest or cell death by phosphorylating Chk2 and p53 on Ser^{15}, stabilizing p53 (*11*), and inducing Chk2-dependent degradation of Cdc25A and blocking S-phase progression by inhibiting Cdk2-dependent DNA synthesis (*9*). In addition, more than 700 substrates are phosphorylated in an ATM-dependent manner, highlighting the complexity of the ATM-mediated cellular response (*16*).

ATM activation is induced by IR treatment, becoming transiently autophosphorylated at Ser^{1981} within minutes of IR exposure and dissipates over a 24-hour period. Glioma stem cells display particularly increased resistance to IR treatment, and this property correlates with increased basal levels and activation of ATM (*12*, *17*). Carruthers *et al.* (*17*) showed that GBM stem cells isolated from different patients displayed a more robust intrinsic phospho-ATM (pATM) signal and radiation induces pATM even further.

Researchers have shown small-molecule inhibitors of ATM to phenocopy ATM loss, including the ability to chemosensitize and radiosensitize cancer cells, although subtle differences have been observed (sister chromatid exchange rates are inhibited by pharmacological inhibition but not in A-T cells) (*18*, *19*). GBM cell lines and GBM stem cells are exquisitely radiosensitized by ATM inhibition in vitro (*20*), and elevated ATM activation has been observed in stem versus differentiated GBM cells (*17*). With an in vivo model system, wherein the non–BBB-penetrant ATM inhibitor KU60019 was pumped directly into mouse brain orthotopic GBM xenograft, it was shown that mutant p53 gliomas exhibited superior ATM inhibitor–mediated radiosensitization compared to matched p53 wild-type gliomas, including prolonged survival of treated mice harboring p53 mutant gliomas relative to isogenic p53 wild-type models (*21*). One-third of GBM tumors contain p53 mutations, and ~80% harbor other cell cycle checkpoint defects including CDKN2A loss (*20*).

In addition to DSB signaling, ATM is activated by surface cysteine residue oxidation at Cys2991 forming a disulfide–cross-linked dimer which subsequently has been shown by cryo-electron microscopy to be in either an open or closed conformation, the latter possibly more active (*22*, *23*). This is potentially relevant to tumor cell mechanisms that protect against reactive oxygen species that are induced over longer periods of time by IR. Finally, reports suggest that ATM deficiency in the normal brain tissue may be radioprotective, as neurons and astrocytes of ATM-deficient mice are radioresistant (*10*, *24*–*26*).This may suggest that a wide therapeutic index exists between inhibiting ATM in the IR-exposed normal brain compared with proliferative and cell cycle checkpoint defective brain tumor tissue.

In collaboration with DDR-focused laboratories around the world, AstraZeneca leads in clinical and preclinical basic research and drug discovery efforts in the DDR therapeutic area (*23*, *27*–*30*) and has previously developed a potent and selective small-molecule ATM inhibitor in clinical development, AZD0156 (*29*) (patent: WO2015/170081) (*31*). AZD0156 is a substrate for efflux transporters and is therefore not likely to significantly cross the BBB. Here, we used novel additional steps in screening cascades to optimize against efflux transporter liabilities. By improving the $K_{\text{p,uu}}$ (the ratio of free plasma/free brain concentration in model systems), we report the discovery of AZD1390, an orally bioavailable ATM inhibitor with excellent physical and chemical properties and greatly improved BBB penetration in the mouse, rat, and monkey compared to AZD0156. We fully disclose here the preclinical primary pharmacology of AZD1390 (patent: WO2017/046216), reporting the in vitro activity and the in vivo pharmacokinetics (PK), pharmacodynamics (PD), and efficacy in combination with radiation in orthotopic and patient-derived xenograft (PDX) brain tumor models. AZD1390 is now in early clinical development as a radiosensitizer of central nervous system malignancies.

RESULTS

The structure and properties of AZD1390

AZD1390 belongs to the same exquisitely potent series of ATM inhibitor as the clinical development compound AZD0156 (Fig. 1). However, AZD1390 was discovered following a series of in vitro assays designed to screen for (i) ATM autophosphorylation activity; (ii) selectivity against closely related PIKK family kinases ATR, DNA-PK, and mTOR activity and (iii) broader kinase panels; and (iv) lack of substrate activity in novel dual-transfected human MDR1 and BCRP efflux transporters assays. AZD1390 was screened against ATM [modulation of purified ATM-dependent phosphorylation of glutathione *S*-transferase (GST)–p53 Ser^{15}] with activity defined as ≥50% [median inhibitory concentration (IC_{50})] of 0.00009 μM (0.00004 μM corrected for tight binding). IC_{50} activity against closely related and purified PIKK family enzymes was never more potent than 1 μM. In broader purified kinase screening panels, AZD1390 was tested at two concentrations, 1 and 0.1 μM, against the Thermo Fisher Scientific kinase panel. At the very high concentration of 1 μM, AZD1390 showed ≥50% inhibition against 3 targets (CSF1R, NUAK1, and SGK), with no activity against the remaining 118 targets tested. At 0.1 μM, no activity was found (<50% inhibition) against 354 kinases. We also tested activity and selectivity of AZD1390 against a panel of kinases run by Eurofins Panlabs. AZD1390 showed activity (>50% inhibition at 1 μM) against 1 kinase, FMS, and showed no activity (<50% inhibition at 1 μM) against 124 other kinases from the panel (Table 1). The IC_{50} against the cardiac ion channel hERG was also confirmed as minimal for both AZD0156 and AZD1390: >33.3 and 6.55 μM, respectively. (A similar IC_{50} for AZD1390 of 7.99 μM against hERG was generated using an alternative assay with improvements in compound handling and data processing).

In cell activity screens, AZD1390 caused inhibition of ATM, as indicated by the inhibition of phosphorylation of $\text{ATM}^{\text{Ser1981}}$ in HT29 cells (used historically and routinely as a consistent cell assay for other projects and selectivity studies) following treatment with irradiation.

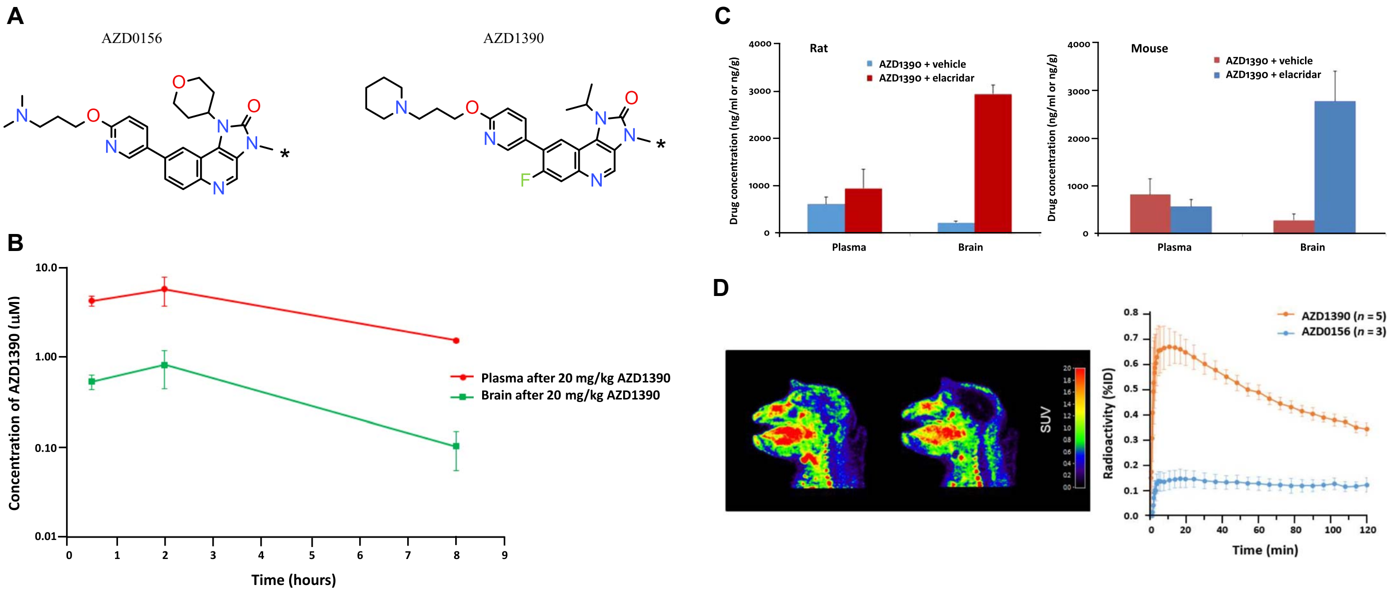

Fig. 1. The structure and brain-penetrating properties of AZD1390. (**A**) Structure of AZD1390 in comparison to clinical ATM inhibitor AZD0156 of the same series. Asterisks indicate positions of carbon-11 label in PET experiments in cynomolgus macaques. (**B**) PK profile of AZD1390 dosed in mouse over an 8-hour period. Concentrations of drug in plasma and brain were measured by liquid chromatography–mass spectrometry (LC-MS). (**C**) Elacridar transporter inhibitor [or GF120918 is a highly potent inhibitor of the ABC (adenosine triphosphate–binding cassette) transporter Pgp and BCRP] or vehicle given intravenously at 10 mg/kg before AZD1390 at 10 mg/kg orally in rat and mouse. Brain and plasma samples were taken 1 hour after dose. (**D**) Color-coded PET images showing distribution of radioactivity in the monkey brain following administration of [^{11}C]AZD1390 (left image) and [^{11}C]AZD0156 (right image). The images represent average radioactivity from 5 to 123 min after injection. Image intensity is displayed as standardized uptake value (SUV), corresponding to the local radioactivity concentration normalized for injected radioactivity and body weight. Both ATM inhibitor compounds were administered to the same monkey on the same day.

The reported IC_{50} values were calculated as the geometric mean of IC_{50} individual values and the arithmetic mean of pIC_{50} values.

BBB penetration

The endothelial cells of the BBB contain efflux transporters MDR1 (Pgp) and BCRP, which serve to actively exclude the compound from the brain (*32*). In vitro efflux assays were set up using Madin-Darby canine kidney (MDCK) cells dual-transfected with human MDR1 and BCRP efflux transporters to identify compounds without substrate activity. In vitro MDCK_MDR1_BCRP studies at both 1 and 0.1 µM suggest that AD1390 is not a substrate for the human Pgp and/or BCRP efflux transporters (efflux ratio, <2); however, it does have a higher efflux rate in rodent species, as lower $K_{p,uu}$ values were observed in rat and mouse (0.17 and 0.04, respectively). This reflects that, in rodents, AZD1390 is seen to be an efflux substrate with increased brain exposure ($K_{p,uu}$, 0.85 and 0.77) on administration of the chemical efflux transporter knockout elacridar (Fig. 1C) and an efflux ratio of 3.2 in the rat transporter-transfected in vitro LLC-PK1-rMdr1a assay at 1 µM. In contrast, AZD0156 at 0.1 µM has an efflux ratio of 23, indicating that it is a human efflux transporter substrate (Fig. 1, B and C). This BBB permeability difference is also reflected in vivo with AZD1390 rat and mouse brain $K_{p,uu}$ values six- and sevenfold higher, respectively, than AZD0156.

Cynomolgus macaque positron emission tomography (PET) images for the two compounds (Fig. 1D) show that only AZD1390 gives significant brain penetration with a C_{max} (%ID) of 0.68 ± 0.078 ($n = 5$) [compare AZD0156 C_{max} %ID 0.15 ± 0.036 ($n = 3$, $P < 0.01$)]. Two-tissue compartment (2-TC) modeling of AZD1390 PET data yielded a V_T (equivalent to K_p) of 5.8 ± 1.2 ($n = 5$) and a calculated $K_{p,uu}$ of 0.33 ± 0.068 ($n = 5$). It was not possible to accurately determine K_p for AZD0156 in cynomolgus macaques. Here, the 2-TC model showed poor identifiability with very high SEs in V_T. We observed lower $K_{p,uu}$ values in rat and mouse for AZD1390 (0.17 and 0.04, respectively). This reflects that, in rodents, AZD1390 appears to be an efflux substrate with increased brain exposure ($K_{p,uu}$, 0.85 and 0.77) on administration of the chemical efflux transporter knockout elacridar (Fig. 3B) and an efflux ratio of 3.2 in the rat transporter-transfected in vitro LLC-PK1-rMdr1a assay at 1 µM. Despite the lower rodent $K_{p,uu}$ values in mouse at 2 to 20 mg/kg, free brain exposure is achieved, with pATM inhibition and efficacy observed.

In vitro ATM target/pathway engagement, radiosensitization, and mechanism of action of cell killing by AZD1390

We next investigated the cellular effects of AZD1390 on the ATM-dependent DDR. Figure 2 (A and B) illustrates that ATM autophosphorylation inhibition by AZD1390 occurred at 4 hours after treatment, and 3 nM produced a strong inhibition of ATM in LN18 GBM cells (other time points were investigated in fig. S1, A to C). Other DDR inhibitors tested under the same conditions at relevant IC_{50} concentrations did not affect pATM levels. After removing AZD1390 and allowing cells to recover, we observed evidence for ATM pathway reactivation at 6 hours as pChk2 levels started to rise (Fig. 2B). To confirm selectivity observed in our cell screens, we also checked for effects on DNA-PK and ATR pathway activation and did not see appreciable effects in Western blots (fig. S1, B and C). Figure 2C shows the effects of AZD1390 added 1 hour before irradiation to NCI-H2228 lung cancer cells (used in subsequent orthotopic brain metastatic in vivo model) in high-content immunofluorescence cell imaging (using the confocal CV7000 imaging microscope) analyzing pATM and γH2AX DDR biomarkers. The median 50% excitatory

Table 1. Properties of AZD1390 in comparison to AZD0156, with BBB permeability differences highlighted. N.D., not determined.

		AZD0156	AZD1390
Potency	ATM cell IC_{50} (μM)	0.00058	0.00078
Selectivity	ATR, PI3K, mTOR, DNAPK, hERG cell IC_{50} (μM)	6.2, 0.61, 1.4, 4.96, >33.3	>30, >12, >16.1, >29.9, 6.55 (7.99*)
Solubility	Solubility (pH 7.4) μM/solid-state assessment	>800 (crystalline)	909 (crystalline)
Permeability and protein binding	Intrinsic permeability (Caco2) Papp A to B 1×10^{-6} cm/s	15.2	$27.1^{\dagger}$
	A to B permeability Papp 1×10^{-6} cm/s/Efflux ratio in MDCK_MDR1_BCRP	N.D. at 1 μM, 1.5/23.4 at 0.1 μM	24.3/1.1 at 1 μM, 16.8/1.8 at 0.1 $\mu M^{\dagger}$
	Brain permeability ($K_{p,uu}$)		
	Mouse (+elacridar)	0.006	$0.04^{\dagger}$ (0.77)
	Rat (+elacridar)	0.027	$0.17^{\dagger}$ (0.85)
	Cynomolgus monkey	ND	$0.33^{\dagger}$
	Protein binding (% free)		
	Rat	11.4	4.2
	Dog	40.9	24.8
	Human	29.0	26.1
In vitro clearance	Hepatocyte CLint (ml/min/1×10^{6})		
	Rat	3.3	7.6
	Dog	3.3	3.2
	Human	5.7	3.9
In vivo PK	Rat CL, Vss, T1/2, F	15.5, 4.3, 4.1, 57%	16.3, 3.0, 2.4, 74%
	Dog CL, Vss, T1/2, F	33.3, 17.6, 7.2, 54%	16.2, 23.7, 21.6, 66%

*AZD1390 IC_{50} activity against hERG using an alternative assay. †Superior permeability and BBB-penetrating properties of AZD1390 over AZD0156.

concentration (XC_{50}) values for AZD1390 using total nuclear staining of pATM and γH2AX are in general agreement with the pATM assay potencies (0.78 nM) reported in the HT29 cell screen (Table 1 and fig. S2A). However, XC_{50} concentrations required to inhibit discreet nuclear pATM foci were higher (2.7 nM) and in agreement with the Western blot data and antiproliferation effects (seen in subsequent results). The data also show that radiation combined with AZD1390 dose-dependently increased the formation of micronuclei—DNA-containing structures indicative of incompletely replicated or broken chromosome fragments. This suggest that AZD1390 results in increased genome instability.

Figure 2D shows the effect of IR and AZD1390 combinations on the cell cycle using NCI-H2228 cells. A dose-dependent increase in G_2 accumulation occurred after 24 hours following AZD1390 and irradiation at 2 Gy indicative of cells not arresting in S and accumulating in G_2 or experiencing problems during mitosis. The data also show a dose-dependent increase in the sub-G_1 population of cells at 48 hours after IR, indicating cells undergoing apoptosis. We also analyzed cell cycle profiles in GBM lines. In 5-ethynyl-2′-deoxyuridine (EdU) pulse-chase experiments across GBM cell lines, with the exception of SW1783 p53 mutant line, T98G and LN18 p53 mutant cells showed higher basal S-phase levels based on DNA content compared with p53 wild-type cells analyzed (fig. S2B). Furthermore, pulse-chase data in LN18 cells indicated that irradiated cells continue to progress through the cell cycle after 48 hours, with minimal accumulation of EdU-positive cells in G_1 phase as compared with T0 (time zero), possibly due to a defect in G_1-S phase arrest in this p53 mutant line. AZD1390 (10 nM) combined with 1- or 2-Gy IR resulted in a shift of population of cells accumulating in G_1 and G_2-M phases rather than in S phase 48 hours following IR (fig. S2C).

Figure 2E shows data from gated cells containing γH2AX foci, pATM foci, and micronuclei at various phases of the cell cycle. This indicates that AZD1390 enhances the accumulation of these DDR biomarkers and facilitates an increase in cells within G_2 and S phases of the cell cycle. Figure 2F shows representative protein expression evidence of a decrease in the IR-induced and ATM-mediated cell cycle checkpoint pChk2 in three GBM cell lines incubated with AZD1390 for 6 hours.

Figure 2G illustrates examples of the level of radiosensitization measured by clonogenic survival achieved with 10 nM AZD1390 as measured by DMR (dose modulation ratio) and DEF at 37% survival in p53 mutant (LN18) and p53 wild-type (DDBRTG5) GBM cell lines. The DEF_{37} for the p53 mutant cell line is 3.0-fold, whereas that for the wild type is 1.2-fold, normalized to dimethyl sulfoxide (DMSO) treatment alone. Table 2 (i) shows the results from clonogenic assays

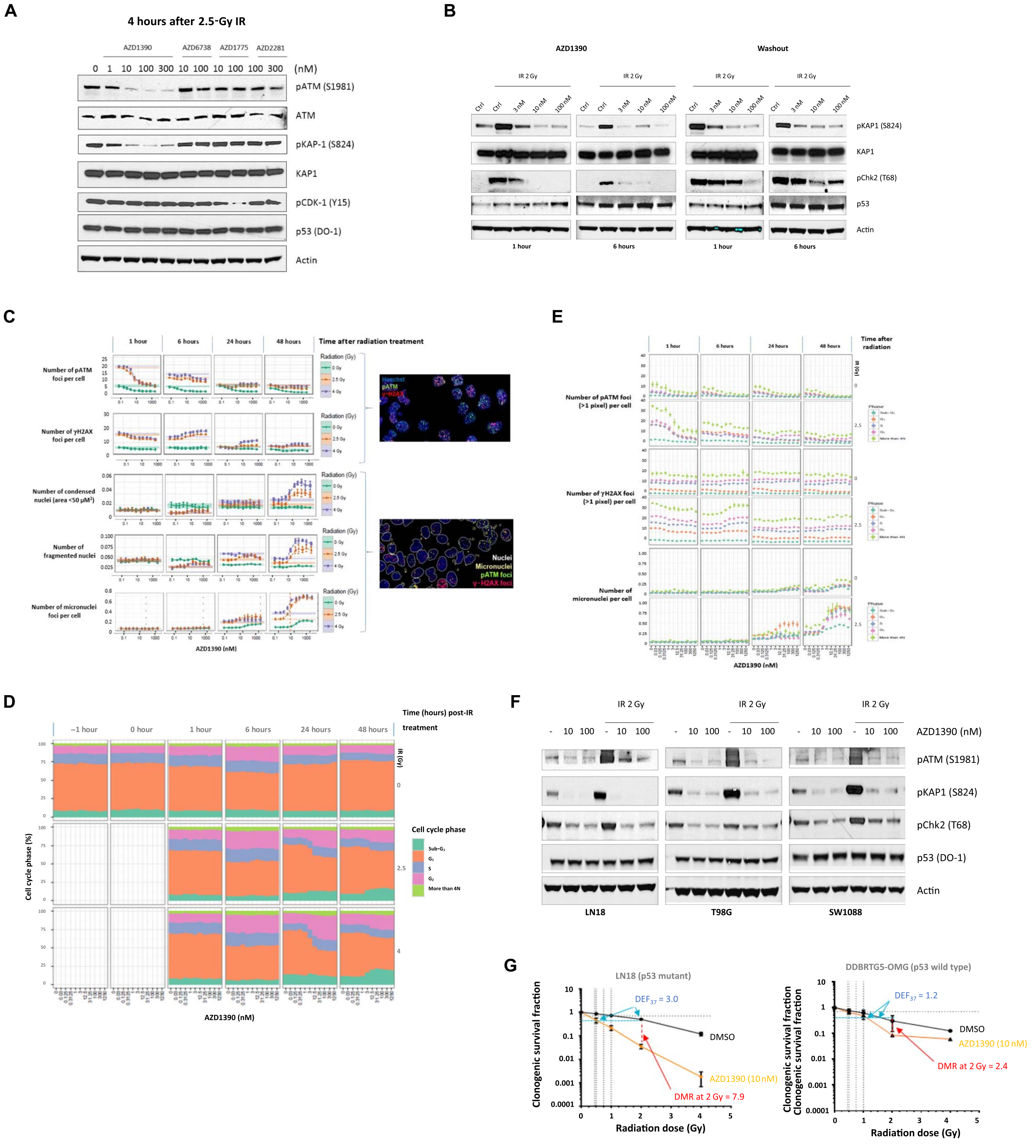

Fig. 2. Target engagement and cellular mechanism of action of AZD1390. (**A**) AZD1390 cellular target engagement using phospho-Ser^{1981} ATM and downstream pathway modulation demonstrating dose-dependent (0 to 300 nM) target engagement (pATM) in LN18 GBM cells at 4-hour time points. Effect of AZD6738 (ATR inhibitor), AZD1775 (Wee1 inhibitor), and AZD2281 (PARP inhibitor, olaparib/Lynparza) selective clinical inhibitors. (**B**) AZD1390 cellular target engagement using phospho-KAP1 (pKAP1) and other downstream biomarkers demonstrating dose-dependent target engagement in NCI-H2228 lung cells after 1 and 6 hours of incubation with drug. A drug-washout time course (right) was used to monitor evidence of pathway reactivation after 6 hours from AZD1390 removal. (**C**) Number of pATM foci, γH2AX foci, and nuclear condensation/fragmentation detected in NCI-H2228 cells by immunofluorescence at various time points following various single doses of IR and effect of dosing AZD1390 before IR exposure in vitro. (**D**) Cell cycle phases as measured by DNA content of NCI-H2228 following 2- and 4-Gy IR at various doses of AZD1390. (**E**) Number of pATM, γH2AX foci, and micronuclei in cells gated by cell cycle phase at various time points after NCI-H2228 cells were treated with 2- or 4-Gy IR at various doses of AZD1390. (**F**) ATM pathway modulation by AZD1390 in three GBM cell lines indicated. Reduction in IR-induced cell cycle checkpoint (pChk2) by AZD1390 after 6 hours of incubation in the drug, confirmed in three p53 mutant GBM cell lines indicated. (**G**) Radiosensitization by AZD1390 (10 nM, orange curves) in p53 mutant and wild-type GBM cell lines in colony formation assays compared to DMSO control (black curves). AZD1390 was added to cells 1 hour before IR and incubated for 10 to 14 days before colonies were counted. *n* = 3, and error bars are SD. DEF$_{37}$, dose enhancement factors at 37% survival.

Table 2. In vitro cellular radiosensitization by AZD1390. (i) Radiosensitization scores across p53 mutant and wild-type cell lines by AZD1390 dosing in clonogenic assays. The lung cell line (NCI-H2228) used for subsequent in vivo brain metastasis models is included. Statistical difference ($P < 0.05$, paired Student's *t* test) between mutant and wild-type scores was observed using both DEF$_{37}$ and DMR at 2-Gy IR. (ii) Radiosensitization scores (DMR) across a broader panel of nine p53 mutant and wild-type glioma cell lines achieved by 10 nM AZD1390 using the Live/Dead antiproliferation assay. Statistical difference ($P < 0.05$, paired Student's *t* test) between mutant and wild-type scores was observed.

(i) Radiosensitization by clonogenicity

Cell line	TP53 status	DEF$_{37}$ 10 nM AZD1390	DMR at 2 Gy 10 nM AZD1390
LN18	Mutant	3.0	7.9
T98G	Mutant	3.9	5.8
NCI-H2228	Mutant	4.0	19.1
A172	Wild type	1.6	1.2
DDBRTG-05MG	Wild type	1.2	2.4
U87MG	Wild type	1.1	1.2
Statistically different (Student's *t* test)		$P < 0.05$	$P < 0.05$

(ii) Radiosensitization by viability

Cell line	TP53 status	DMR at 2 Gy 10 nM AZD1390
LN18	Mutant	27.5
T98G	Mutant	21
HS683T	Mutant	10.3
SW1088	Mutant	46.1
SW1783	Mutant	3.7
DDBRTG-05MG	Wild type	1.0
CCF-STTG1	Wild type	1.0
A172	Wild type	0.8
U87-MG	Wild type	5.2
Statistically different (Student's *t* test)		$P < 0.05$

reported in other glioma cell lines and demonstrates that p53 wild-type representatives fall into the statistically less radiosensitive category. Figure S3A shows the radiosensitization achieved across a dose range of AZD1390. In a broader glioma-derived panel of p53 mutant versus wild-type cell lines, we also tested AZD1390-mediated radiosensitization across nine glioma lines using a higher-throughput antiproliferation assay (Table 2, ii). This assay detects viable cells in in vitro 5-day Live/Dead growth assays, and the results indicated that all p53 wild-type cells were statistically less radiosensitized than p53 mutant cells tested, which supports previous reports that p53 status directly affects the radiosensitization of GBM cells by ATM inhibition (*21*). Figure 3B shows representitive curve shifts of these data.

PD and PK of AZD1390 in vivo

We performed an extensive assessment of the relationship between PK and PD of AZD1390 in plasma, brain, and tumor samples from our orthotopic brain tumor model, NCI-H2228, implanted in the brain. The data show that the combination of pharmacologically active doses of AZD1390 from the in vitro and cell potency assays inhibited the IR-induced PD biomarkers pATM (Ser^{1981}) and phospho-Rad50 (pRad50) (Ser^{635}) in vivo in a dose- and time-dependent manner (Fig. 3, A and B). The antibody used to detect the latter is being used in clinical trials, and the data in Fig. 4B show the staining levels correlating with PK observations in Fig. 2A. The combination of AZD1390 with IR also significantly increased the apoptotic marker CC3 (cleaved caspase-3) compared to IR alone in NCI-H2228 lung cancer brain metastasis (LC-BM) model, suggesting that the combination is inducing tumor cell death (Fig. 3C). The data reveal a correlation between PK and PD modulation, with AZD1390 free brain levels peaking within 1 hour of dosing and dissipating over a 24-hour period, correlating with ATM inhibition activity (see fig. S4, A and D, for further details on PK and PD analyzed).

In vivo efficacy

We next performed a series of efficacy studies using a lung NCI-H2228 xenograft model either implanted into nude mice brains directly (intracranial brain) or injected into the carotid artery [intracarotid artery (ICA)] and allowed to establish in the brain. Figure 4A shows data that demonstrate a dose-dependent tumor growth inhibition (TGI), with marginal inhibition observed using AZD1390 (5 mg/kg) dosed an hour before each daily fraction of IR. Superior efficacy was observed dosing at 20 mg/kg once daily (QD) or twice daily (BID) in combination with the four daily fractions of IR. The data show the survival of the same mice. Figure S5 (A and B) shows a repeat experiment using BID dosing.

Figure 4B uses the same model, but this study includes the addition of TMZ, the standard of care adjuvant chemotherapy used for the treatment of glioblastoma. This study shows AZD1390 dosed at 15 mg/kg (we had to drop the dose from 20 mg/kg to achieve a tolerated triple combination of AZD1390, IR, and TMZ). TMZ (25 mg/kg) provides the equivalent exposure used in the clinic. This treatment [triplet AZD1390 (15 mg/kg) + 2 Gy × 5 IR + TMZ (25 mg/kg)] was tolerated (body weight data in fig. S6E) and provided additive TGI and survival benefit over the AZD1390 (15 mg/kg) + IR doublet arm. However, based on previous and subsequent studies, this additive effect is comparatively no more beneficial than that achieved with the doublet of AZD1390 (20 mg/kg, QD) + 2 Gy × 5 IR.

We also used a model that represents brain metastasis by ICA injection of NCI-H2228 cells and tumor establishment in the brain. Figure 4C shows AZD1390 + IR effects on the effect of TGI in this model (ICCIN-2026) and showed that this model also responded. This translated into animal survival benefit in a dose-dependent manner.

We also used a syngeneic mouse model of GBM by testing AZD1390 in combination with stereotactic radiation in the previously published GL261 orthotopic model (*21*). Figure 5A shows survival of animals dosed with AZD1390 (20 mg/kg) combined with 2 × 5 Gy focal beam IR fractions using a third orthotopic mouse model, in which we implanted murine syngeneic GL261 GBM cells directly into immunocompetent (C57 Black 6) mice. Dosing AZD1390 in this model resulted in a significant response to 20 mg/kg QD combined with just two fractions of 5-Gy focal beam (stereotactic) radiation compared to IR or AZD1390 alone arms. Lowering the dose of AZD1390 to 5 mg/kg QD resulted in reduced efficacy, establishing a dose-dependent effect in this immunocompetent syngeneic model (Fig. 5B). However, this study also increased the number of

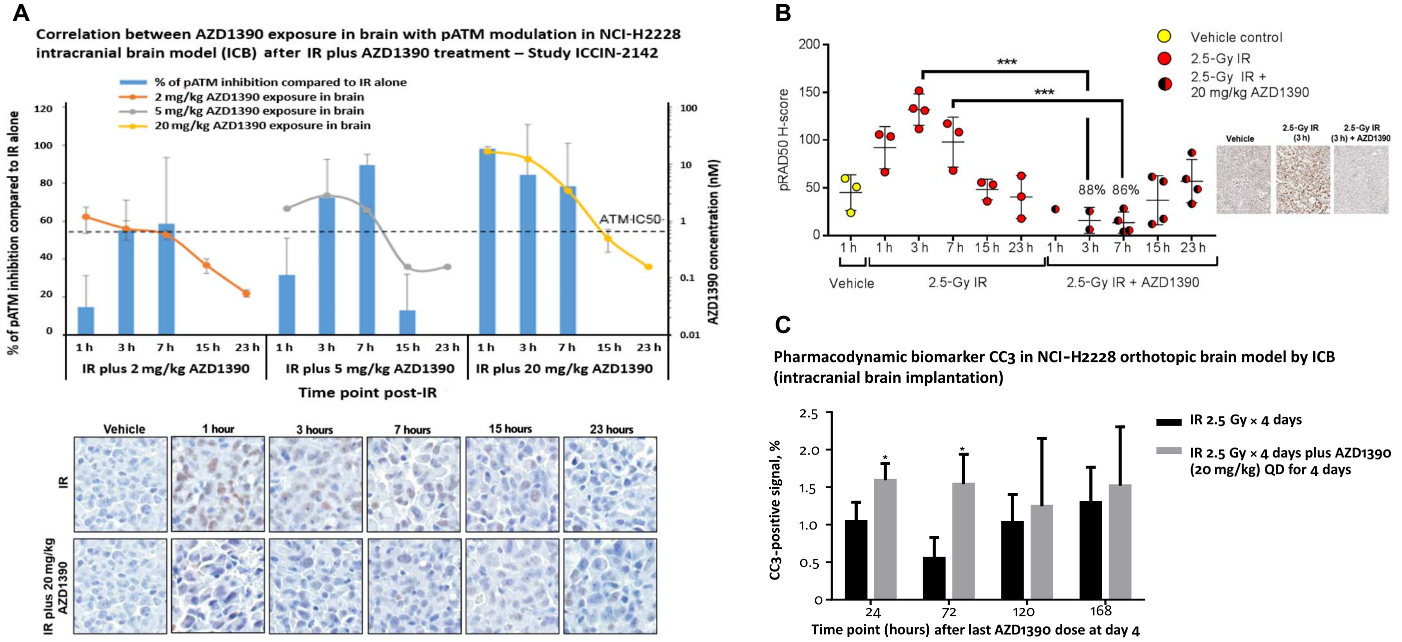

Fig. 3. Pharmacokinetics and pharmacodynamics of AZD1390. (**A**) Correlation between free brain exposures of AZD1390 (PK) with PD modulation of pATM (Ser^{1981}) in NCI-H2228 orthotopic lung-brain tumor model. Lower panel shows associated IHC PD images taken at various time points following IR ± AZD1390 (20 mg/kg). (**B**) pRad50 (Ser^{635}) modulation following IR ± AZD1390 (20 mg/kg), with right panel showing representative IHC images (fig. S4B shows, in more detail, the scoring criteria for staining using this clinically validated pRAD50 IHC antibody). (**C**) Induction of apoptosis as measured by CC3 staining in the above tumor samples. Error bars indicate SD.

fractions to 10 fractions of 2 Gy, which, without addition of AZD1390, marginally improved survival compared to just two fractions.

Finally, we tested AZD1390 in six PDX models of TMZ-sensitive and TMZ-resistant GBM, with two models being p53 mutant. In agreement with our in vitro data, some p53 wild-type models responded better than others (Fig. 6). The survival data generated in this small panel of PDX models do not segregate response based on p53 status alone. However, both the p53 mutants were among the best responding models to AZD1390 in combination with radiation, while the least responding model was p53 wild type (ST2473).

DISCUSSION

By deploying in vitro human efflux transporter screening assays and chemical evolution from the potent AZD0156 inhibitor scaffold, we have developed a BBB-penetrant ATM kinase inhibitor, AZD1390, and begun clinical development. The BBB penetration of AZD1390 was confirmed here using non–human primate PET imaging of ^{11}C-radiolabeled AZD1390. While not being a significant substrate for efflux transporters such as Pgp and BCRP, AZD1390 retains exquisite ATM potency and selectivity. Although at the high concentration of 1 μM, AZD1390 showed ≥50% inhibition against three targets (CSF1R, NUAK1, and SGK), with no activity against the remaining 118 targets tested, this extremely high exposure is not required in the clinic for therapeutic radiosensitization because the concentrations required in vitro were maximal at 10 nM. CSF1R is a potentially attractive target to inhibit in the brain to prevent demyelination with CSF1R-targeting agents in phase 1 trials (*33*). NUAK and SGK have been linked to roles in Myc-driven tumorigenesis and cancer cell resistance to cellular stress (*34*), but their function in the brain, if any, is not well defined.

AZD1390 has favorable physical, chemical, PK, and PD properties suitable for clinical applications that require exposures within the central nervous system. We show that AZD1390 potently inhibits ATM kinase activity in vitro (cellular IC_{50} ranging from 0.5 to 3 nM depending on the assay used), modulates the DDR, and sensitizes tumor cells of GBM and lung origin to radiation. We show that AZD1390 preferentially radiosensitizes p53-deficient GBM cell lines, which supports previous findings using tool ATM kinase inhibitors (*21*). Recently, in collaboration with the same authors, we showed that this may be due, in part, to an inability of p53-deficient cells to arrest after IR-induced DNA damage and that ATM inhibition exacerbates this by blocking the repair of DSBs and causing cell death by mitotic catastrophe (*35*). Our data here using immunofluorescence imaging showed exacerbation of micronuclei formation by AZD1390 in combination with radiation, in vitro supporting this notion. A dose-responsive increase in γH2AX occurred at an earlier time point of 6 hours after IR exposure mostly in cells with 4N and in G_2 phase and went away soon after, while later time points (24 and 48 hours) showed increases in micronuclei formation, again in cells with 4N DNA or not only in G_2 but also in sub-G_1 cells where cell death is likely to be occurring. We also observed that AZD1390 prevented the IR-induced and ATM-dependent phosphorylation of Chk2 in GBM cells, which supports the observation that AZD1390 combined with IR causes NCI-H2228 cells to continue cycling through the S phase, accumulates damage in the G_2 phase, and undergoes gross genomic instability, micronuclei formation, and apoptosis during catastrophic mitosis.

We show that AZD1390 dose-dependently engages ATM target and pathway in vitro and in vivo and have established a PK-PD-efficacy relationship that models the exposures required to achieve significant and prolonged orthotopic TGI and survival benefit. We used a variety of immunohistochemical (IHC) antibodies to study PD of the ATM and apoptotic pathway, and all indicated that inhibition above the cellular IC_{50} potency against ATM for 3 hours or more in combination with fractionated radiation in vivo is sufficient to block tumor growth and

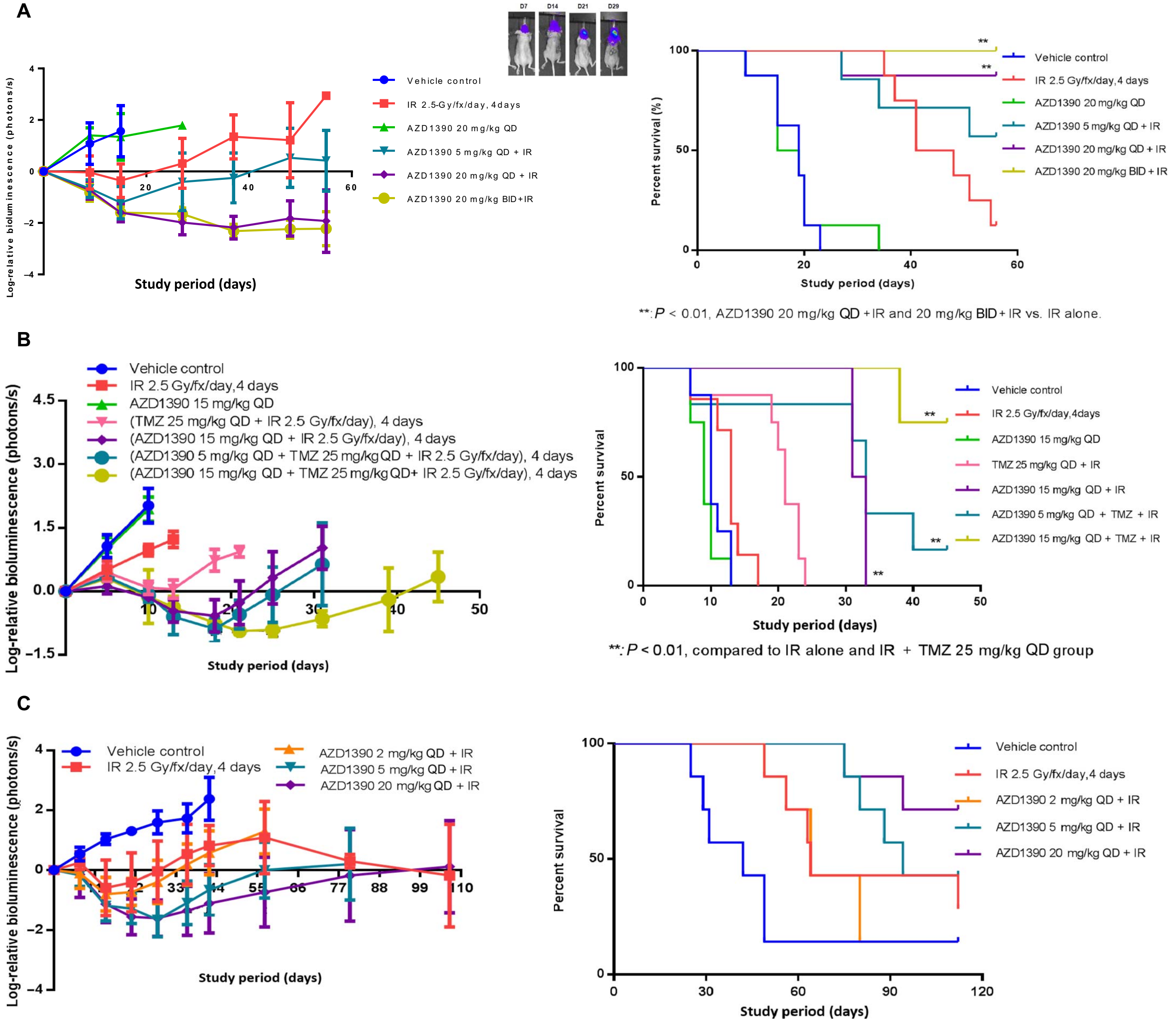

Fig. 4. In vivo activity of AZD1390 in lung-brain metastatic models. (**A**) Tumor growth was measured by bioluminescence, with inset images showing tumor growth rate measured using a Xenogen IVIS-200 imaging system from the start of treatment and assessed by the mean change in bioluminescence intensity. The first panel represents tumor growth relative to control background signal and associated survival plots shown using AZD1390 in combination with IR in the NCI-H2228 intracranial injection into the brain (ICB) model. The same animals used for tumor growth were assessed for survival in the second panel. (**B**) The first panel represents tumor growth effects as measured by bioluminescence relative to control background signal and associated survival plots using AZD1390 in combination with IR and TMZ in the NCI-H2228 ICB model. The same animals used for tumor growth were assessed for survival in the second panel. (**C**) The first panel represents tumor growth effects as measured by bioluminescence relative to control background signal and associated survival plots using AZD1390 in combination with IR in the NCI-H2228 ICA model. The same animals used for tumor growth were assessed for survival in the second panel.

improve survival in animal orthotopic brain models of both GBM and LC-BM. Although the combination of AZD1390 with IR significantly increased the apoptotic marker CC3 compared to IR alone in NCI-H2228 LC-BM model, suggesting that tumor cell death is being induced by the combination (Fig. 3C), the levels of induction were smaller than those for the ATM-dependent biomarkers and the TGI observed. This could reflect that not all tumor cells are undergoing apoptosis at the early time points of 24, 48, 120, and 168 hours analyzed and that cell death occurs after several days in vivo compared to our in vitro analyses on the sub-G_1 population, where doubling times of cells are often faster than when growing in vivo (tumors doubled in size in approximately 10 days compared to 2 to 3 days for cells to double in number in vitro).

We used intracranially implanted xenografts by carotid artery injection, which subsequently led to brain tumor establishment. We performed implantation via carotid artery injection to technically avoid any physical disruption to the BBB. We did notice some variability in tumor growth rates and survival between studies using the same intracranially implanted model (ICB) in the control arms on different occasions. Although a strong correlation between luciferase-measured growth rate and survival was noted, the discrepancy between studies may be indicative of tumor cells being implanted in slightly different sites within the brain (despite tumor cells always being injected into the same cerebral hemisphere in the ICB models). This may cause variation in the tumor microenvironment and/or migration into critical parts of the brain that might affect moribund status. However, the control arms enabled the comparative assessment of benefit afforded by the treatment of radiation and/or AZD1390. We also tested whether TMZ had any effects on their own or in combination with the doublet treatment of AZD1390 and radiation. We had to reduce the concentration of AZD1390 to achieve a tolerated triplet combination maintaining the TMZ dose that is the equivalent of that used in the clinic (see fig. S6, B to E, for body weight measurements). Notably, no overt behavioral symptoms were observed in any of the AZD1390 combined with radiation treatment arms. This model responded to the addition of TMZ, and the triplet combination showed an improvement over the doublet. However, our other studies performed without TMZ showed that this additive effect of TMZ is comparatively no more beneficial than that achieved with a doublet of AZD1390 (20 mg/kg, QD) + 2 Gy × 5 IR. The case for a tolerated triplet combination remains open at this time.

Table 3. PDX models with p53 and clinical TMZ sensitivity status used for subcutaneous explant studies.

Model	p53 status	TMZ sensitivity
ST108	TP53 G2455	Resistant
ST112	TP53 R273H	Resistant
ST146	Wild type	Resistant
ST545	Wild type	Resistant
ST610	Wild type	Sensitive
ST2473	Wild type	Sensitive

Because these studies were carried out using whole-brain radiation, we also undertook to observe any normal brain tissue effects of radiation with and without dosing of AZD1390. Earlier work performed in the McKinnon laboratory (*10*, *26*) supported the notion that inhibition of ATM (genetic ablation) might actually protect the normal brain from the adverse effects of radiation. While inherited ATM deficiency results in neurodegeneration and cerebellar ataxia, ATM has been shown to promote radiation-induced apoptosis in both normal postmitotic and neural stem cell (NSC) populations and that neurons and astrocytes of ATM-deficient mice are radioresistant (*10*, *26*). More recently, Jeggo and colleagues have shown that ATM mediates apoptotic cell death in SVZ cells after low doses of radiation and that NSC populations in ATM-deficient embryos and adult mice exhibit radioresistance (*24*, *25*). In the same mouse brain PD samples that were exposed to a single dose of 2.5-Gy IR, we counterstained with hematoxylin and scored for pathological changes in the surrounding cortex (fig. S6, A and B). We did observe a statistically significant increase in brain tissue lesions after 1 hour of a 2.5-Gy IR exposure, which fell back to healthy normal levels as quickly as 3 hours after IR. In mice dosed with AZD1390 (20 mg/kg), however, the initial 1-hour increase was not observed, which might suggest that some level of neuroprotection may have been afforded, although, due to low scorable sample number in this treatment, statistical analysis was not possible. We did observe slightly increased levels of lesions in normal brain tissue at 3 to 15 hours after IR in the AZD1390-treated brain samples, which did return to normal levels after 23 hours. Caution has to be taken regarding these data, as levels, even if significant, may not be large or durable enough to be translated into any symptomatic clinical signs. We did not observe any abnormal behavioral signs in the mice on study, and the body weights measured did not change during prolonged in vivo studies in mice treated with the combination of radiation and AZD1390 (see fig. S6, C to F). The mice receiving both AZD1390 and radiation were the only ones to maintain weight compared to control arms in which tumor growth continued.

Finally, we tested AZD1390 in combination with radiation in PDX models grown subcutaneously. These GBM models were derived from patients that were TMZ-resistant or TMZ-sensitive and correlated with O6-methylguanine-DNA methyltransferase (MGMT) gene expression status (fig. S7, A and B) and either p53 wild type or p53

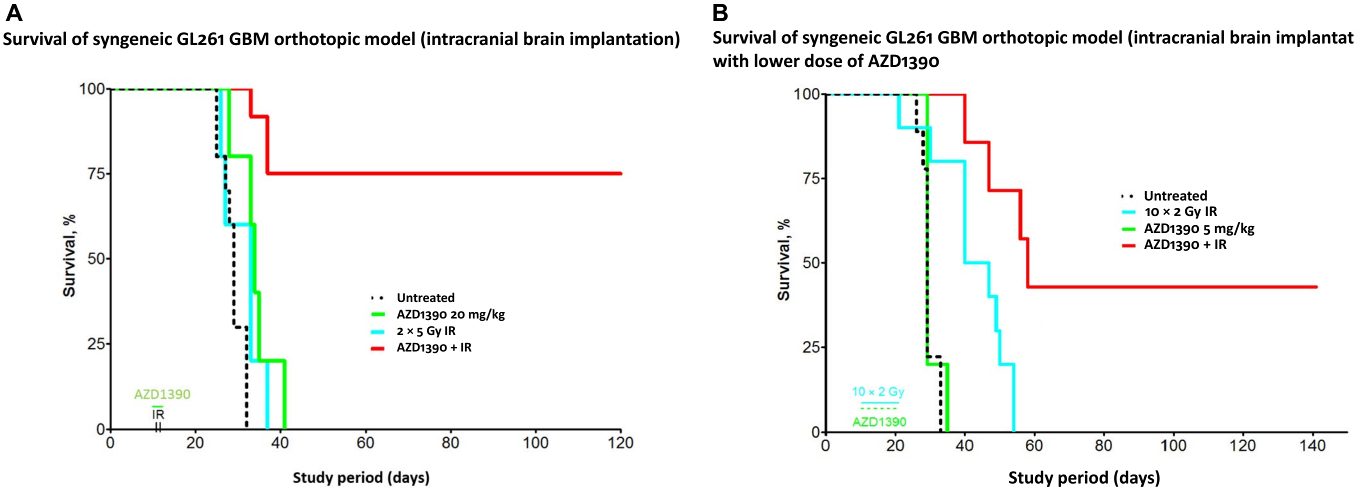

Fig. 5. Survival of a syngeneic mouse model of GBM treated with AZD1390. (**A**) Survival of GL261 tumor-bearing mice dosed with AZD1390 (20 mg/kg) plus 2 × 5-Gy focal beam IR delivered by small-animal radiation research platform (SARRP). (**B**) Survival of GL261 tumor-bearing mice dosed with AZD1390 (5 mg/kg) plus 10 × 2-Gy focal beam IR ($P = 0.0006$ for AZD1390 + IR versus IR alone).

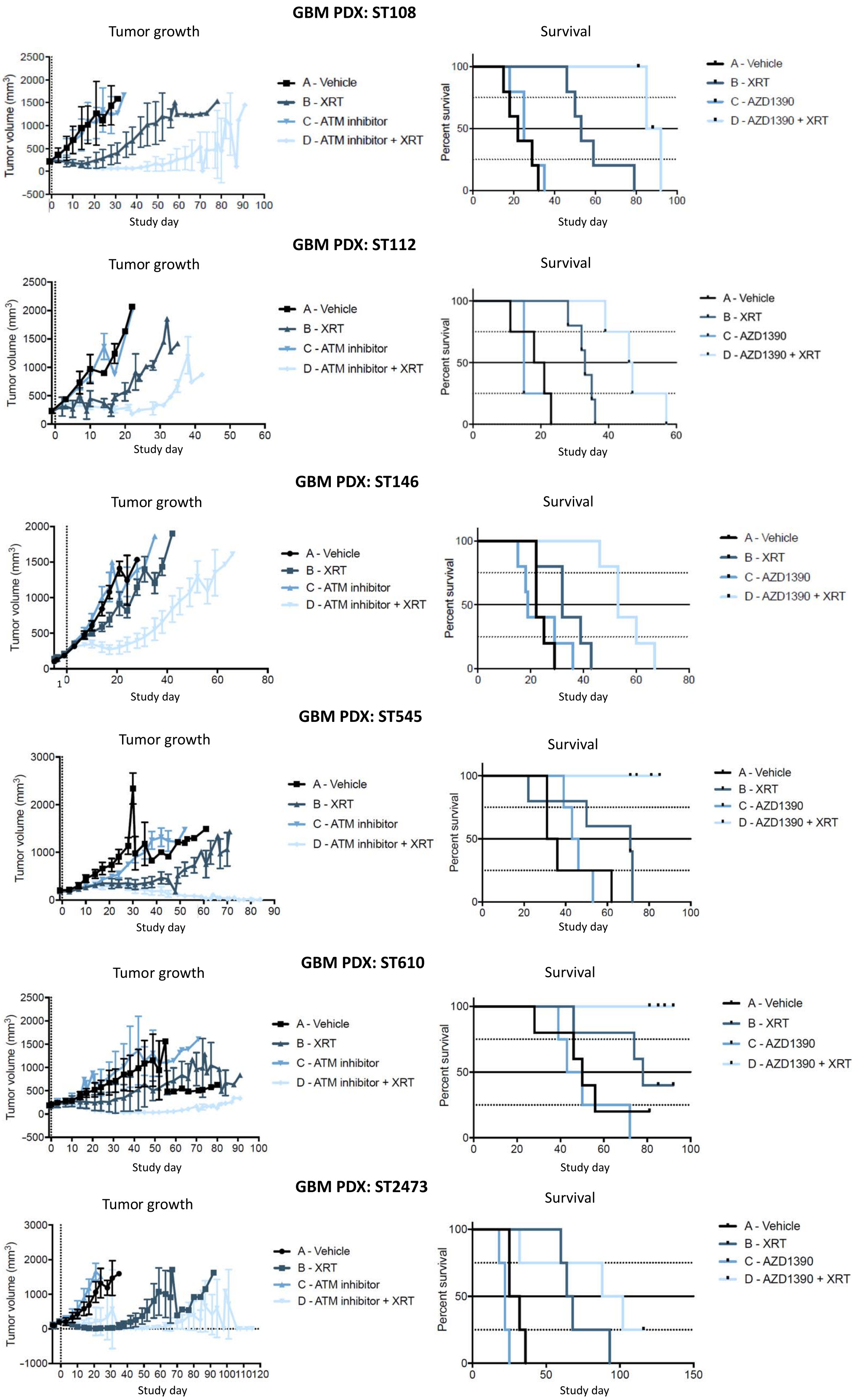

Fig. 6. In vivo subcutaneous efficacy studies using PDX models. Mice were shielded from radiation except for the tumor region and exposed to 2 Gy × 5 days of IR [x-ray therapy (XRT)] and dosed QD with vehicle or AZD1390 1 hour before IR. Tumor growth (left column) and survival (right column) were indicated.

mutant. Both the p53 mutant PDX models tested were among the models most responsive to AZD1390 in combination with radiation, while the least responsive model was p53 wild type (ST2473) (fig. S7), which supports our in vitro data and that of previous studies in the Valerie laboratory (*20*, *21*). However, several p53 wild-type models also responded well, and as concluded in the in vitro analysis undertaken here, it is likely that other genetic or epigenetic factors contribute to the response of irradiated cells to ATM inhibition. The caveat of comparing these models is that some of the p53 wild-type PDX models did not grow as well as others, which makes response comparisons challenging. On the basis of these data and previous publications using isogenic p53 models, the p53 status of patient GBM samples will be looked at retrospectively in the phase 1 trial (NCT03423628) and may be used to develop criteria for patient stratification in future trials.

In all of the above in vivo efficacy studies, one cycle of 10 Gy in total radiation was delivered as fractions either to the flank subcutaneous tumor, by whole-brain radiation exposure, or as focal beam (stereotactic) radiation exposure by SARRP to the brain tumor implant region. Each method resulted in remarkable and robust TGI and, in some studies, resulted in 100% survival benefit of animals over the time of study indicated, compared to radiation alone–treated animals. This is encouraging considering that these results were achieved with only limited numbers of clinically dose-relevant radiation fractions.

On the basis of the preclinical data reported here, AstraZeneca is now supporting early clinical development of AZD1390, including a phase 1 PET imaging study in healthy volunteers to assess brain exposures of microdosed ^{11}C-labeled AZD1390 (ClinicalTrials identifier: NCT03215381) and an oncology phase 1 trial in combination with standard of care radiotherapy in patients with GBM and brain metastases from solid tumors (ClinicalTrials identifier: NCT03423628).

MATERIALS AND METHODS

Western blotting

Cells were seeded in six-well plates to a density of 50 to 60% and incubated at 37°C for 24 hours. Cells were pretreated with AZD1390, the ATR inhibitor AZD6738, the Wee1 inhibitor AZD1775, the poly(adenosine diphosphate–ribose) polymerase (PARP) inhibitor olaparib, or the DNA-PK inhibitor KU-0060648 at indicated concentrations for 1 hour and subsequently irradiated at 2 Gy using the Faxitron CellRad (130-kV, 5-mA, 0.5-mm Al). In washout experiments, cell culture medium was immediately replaced and cells were incubated with or without the compound for 1, 6, and 24 hours. In all other experiments, proteins were collected at indicated time points following irradiation. Proteins were harvested by scraping the cells in radioimmunoprecipitation assay (RIPA) lysis buffer (Millipore) supplemented with protease and phosphatase inhibitors. Protein content was quantified using the BCA Protein Assay Kit according to manufacturing conditions (Thermo Fisher Scientific #23225). Proteins were separated by SDS–polyacrylamide gel electrophoresis on 4 to 12% bis-tris or 3 to 8% tris-acetate gels and transferred onto nitrocellulose membranes using the iBlot Dry Blotting System (Life Technologies). Membranes were briefly washed with water and tris-buffered saline (TBS) with 0.05% Tween 20 (TBST) once and incubated in blocking solution, followed by primary antibodies diluted in TBST with 5% (w/v) nonfat dry milk or 3% bovine serum albumin (BSA) overnight at 4°C with shaking. Membranes were then washed three times and incubated for 1.5 hours with horseradish peroxidase (HRP)–conjugated antibodies and/or LI-COR fluorescent antibodies CW700-800 in TBST with 5% (w/v) nonfat dry milk. Membranes were washed five times with TBST, and proteins were visualized with the Fuji or Syngene G:BOX Imaging System or Film Developer after enhanced chemiluminescence substrate addition. Primary antibodies used were anti-ATM pS1981 (ab81292), anti-ATM (ab78), anti-KAP1 pS824 (ab70369), and KAP1 (ab10483) from Abcam; anti-CHK2 pT68 (#2661), anti-CHK1 pS345 (#2348), anti-CHK1 (#2360), anti–DNA-PKcs (#12311), and anti-GAPDH (glyceraldehyde-3-phosphate dehydrogenase) (#2118) from Cell Signaling Technology (CST); and anti-CHK2 (05-649) from Merck Millipore. Anti–DNA-PKcs pS2056 was generated in-house.

Fluorescent in-cell imaging of DDR pathway modulation

NCI-H2228 cell line was routinely cultured in RPMI 1640 (R0883, Sigma-Aldrich) with 1% L-glutamine (25030-024, Gibco), 10% fetal calf serum (10270, Gibco), and 1% penicillin-streptomycin (P0781, Sigma-Aldrich). NCI-H2228 cells were tested and shown to be mycoplasma-free.

Cells (3000 per well) were seeded in a 384-well format (CellCarrier Ultra, PerkinElmer) in RPMI with 10% fetal bovine serum. After 24 hours, plates were Echo-dosed with a semi-log dose dilution of each compound from a top concentration of 1250 nM. One hour after compound dosing, plates were irradiated with 0, 2.5, or 4 Gy. At 1, 6, 24, and 48 hours after irradiation, plates were fixed by adding a 1:1 volume of 8% paraformaldehyde (PFA) directly to the medium to give a final concentration of 4% PFA and incubated for 30 min at room temperature before washing three times with phosphate-buffered saline solution (PBSA); plates were stored at 4°C. Cells were permeabilized and blocked with modified blocking buffer (PBSA with 1.1% BSA and 0.1% Triton X-100) for 1 hour at room temperature. The modified blocking buffer was aspirated from each well, and primary antibodies against pATM (Rb; Millipore; MAB3806; 1:10,000) and γH2AX (Ms; CST; 25775; 1:400) were added in modified blocking buffer and incubated overnight at 4°C. Primary antibodies were removed, and cells were washed three times with PBSA before incubation with secondary antibodies for 1 hour at room temperature—goat anti-mouse 488 (Life Technologies; A11001; 1:500), goat anti-rabbit 555 (Life Technologies; A21429; 1:500), and Hoechst (Life Technologies; H3570; 1:1000). Secondary antibodies were removed, and cells were washed three times with PBSA and stored with PBSA (75 μl per well) with ProClin before imaging on a Yokogawa CV7000 microscope. For imaging, confocal capture at ×20 magnification of six fields of view with an exposure of 250 ms and *z*-offset of −3 μm for each of the three channels: 405 (BP445/45), 488 (BP525/50), and 561 (BP600/37) for excitation and acquisition wavelengths, respectively. Image analysis was done using Columbus image analysis software (PerkinElmer) and data analysis using R.

Colony formation and Live/Dead assays

The colony formation assay was selected as it measures the replicative potential of cells in vitro and provides a sensitive measure of the impact of long-term effects of radiation on a cell's ability to replicate. Cells were seeded at low density and pretreated with AZD1390 before irradiation. Plates were incubated for 12 to 14 days. The medium was removed, and colonies were stained with crystal violet methanol mix. Colonies were counted on the GelCount. Cell survival was calculated relative to nonirradiated controls and normalized to compound treatment alone. DEF values were calculated as the ratio of doses to produce 37% survival (DEF_{37}) in Prism. The average DEF_{37} values for drug-induced sensitization were calculated from second-order polynomial curve fits through the dose-response data (log survival versus radiation dose) of the individual experiments and presented in Fig. 2—errors on DEF_{37} are SD.

Higher-throughput Live/Dead antiproliferation assay was used across broader cell line panels. Viable cells were scored at day 5 in 384-well plates. SYTOX Green working solution (8 μl) was added to each well (v = 100 μl) and incubated for 1 hour at room temperature, and plates were then read on an Acumen laser scanning plate reader on a program set to detect the number of SYTOX Green–stained cells. The total fluorescent intensity across the well was then read, and the number of dead cells was calculated by dividing the total fluorescence by the fluorescence of a single cell. After counting dead cells, 16 μl of 0.25% saponin (in TBS/EDTA and 0.22 μm filtered) was added to each well. Plates were incubated at room temperature for 16 hours to ensure suitable permeabilization of the cells and staining with SYTOX Green, and a re-read on the Acumen was performed to provide a total cell count. A live cell count was determined by subtracting the dead cell count from the total cell count. Raw data from Acumen were processed in Excel and in GraphPad Prism to generate concentration required for 50% growth inhibition (GI_{50}) values and response curves.

In vitro human efflux transporter

Human MDR1–transfected MDCK cells (MDCK_MDR1) were obtained from the Netherland Cancer Institute. This cell line was transfected with human BCRP internally (AstraZeneca, Innovation Center China, Shanghai). MDCKII-MDR1-BCRP cells were seeded onto polyethylene membranes (PET) in 96-well insert systems at a density to form a confluent cell monolayer. Test and reference compounds were diluted with the transport buffer (Dulbecco's modified Eagle's medium, Invitrogen) to a concentration of 1 or 0.1 μM. The final percent volume of the organic solvent was less than 1%. Permeation of the test compounds from A to B direction and from B to A direction was determined over a 90-min incubation at 37°C and 5% CO_2 with a relative humidity of 95%. At the end of the incubation, samples from the apical and basolateral side were taken and then precipitated with cold acetonitrile containing internal standard. After centrifugation at 4000 rpm, the supernatant was diluted with 0.1% formic acid aqueous solution and analyzed by LC-MS/MS. The integrity of the cell monolayers was confirmed by using the marker Lucifer yellow.

The permeability coefficient (1×10^{-6} cm/s) was calculated using the following equation

$$\mathrm{Papp} = (\mathrm{d}C_\mathrm{r}/\mathrm{d}t) \times V_\mathrm{r}/(A \times C_0) \tag{1}$$

The efflux ratio was calculated using the following equation

$$\text{Efflux ratio} = \text{Papp(B to A)}/\text{Papp(A to B)} \tag{2}$$

where $\mathrm{d}C_\mathrm{r}/\mathrm{d}t$ is the cumulative concentration of the compound in the receiver chamber as a function of time (in μM/s); V_r is the solution volume in the receiver chamber (0.1 ml on the apical side and 0.3 ml on the basolateral side); A is the surface area for the transport, that is, 0.11 cm^2 for the area of the monolayer; and C_0 is the initial concentration in the donor chamber (in μM).

Efflux ratios were also determined in a rat Mdr1a–transfected cell line LLC-PK1-rMdr1a at 1 μM following a 120-min incubation measured at Solvo Biotechnology.

Mouse plasma and brain bioanalysis of AZD1390 by MS

Institutional Review Board and/or Institutional Animal Care and Use Committee guidelines were followed with animal subjects. Each plasma sample (25 μl) was prepared using an appropriate dilution factor and compared against an 11-point standard calibration curve (1 to 10,000 nM) prepared in DMSO and spiked into blank plasma. Acetonitrile (100 μl) was added with the internal standard, followed by centrifugation at 3000 rpm for 10 min. The supernatant (50 μl) was then diluted in 300 μl of water and analyzed via ultraperformance liquid chromatography (UPLC)–MS/MS.

The brain was weighed in fast preparation tubes containing Lysing Matrix A (MP Biomedicals). Water was added as a base for homogenization (two times, w/v). Homogenization was carried out in FastPrep-24 5G (MP Biomedicals) at 6 m/s for 30 s, twice.

Each tumor homogenate sample (25 μl) was compared against an 11-point standard calibration curve (1 to 10,000 nM) prepared in DMSO and spiked into blank tumor homogenate. Acetonitrile (100 μl) was added with the internal standard, followed by centrifugation at 3000 rpm for 10 min. The supernatant (50 μl) was then diluted in 300 μl of water and analyzed via UPLC-MS/MS.

Brain and plasma binding of AZD1390

Rat brain binding (fu_{brain}) was determined using the rat brain slice binding method, as detailed by Fridén *et al.* (*36*). Plasma binding (rat, mouse, dog, monkey, and human) was determined by equilibrium dialysis using a rapid equilibrium device (Thermo Fisher Scientific). The compound in plasma at 1 or 0.1 μM was dialyzed with buffer at pH 7.4 and 37°C for 16 hours. After incubation, aliquots of both plasma and buffer were added to equal volumes of blank buffer and plasma, respectively, before precipitation with acetonitrile prior to centrifugation and analysis of the supernatants by UPLC-MS/MS. Fu_{plasma} was determined by dividing the concentration in the buffer chamber by the concentration in the plasma chamber.

Rodent brain/plasma ratio K_p and $K_{p,uu}$ for AZD1390

Six male Han Wistar rats were dosed at 10 mg/kg orally using a suspension formulation of 0.5% hydroxypropyl methylcellulose (HPMC) + 0.1% (v/v) Tween 80 in water. Brain and blood samples were collected at 0.5, 1, 2, 4, 7, and 16 hours after dose. Plasma was generated by centrifuging the blood samples for 5 min at 5000 rpm. Brain tissue was homogenized following addition of three times the volume of phosphate-buffered saline (pH 7.4). Quantification of the compound in plasma and brain was undertaken by LC-MS/MS following precipitation with acetonitrile. Area under the curve (AUC) was determined from 0 to 16 hours in the brain tissue and plasma, and the brain/plasma ratio K_p was determined using the equation

$$\text{Brain } K_\mathrm{p} = \mathrm{AUC}_{0-16\mathrm{brain}}/\mathrm{AUC}_{0-16\mathrm{plasma}} \tag{3}$$

Unbound brain to plasma ratio was determined using the equation

$$\text{Brain } K_\mathrm{p,uu} = K_\mathrm{p} \times \mathrm{fu}_\mathrm{brain}/\mathrm{fu}_\mathrm{plasma} \tag{4}$$

Mouse brain K_p and $K_\mathrm{p,uu}$ were determined as for the rat study at 10 mg/kg but using 12 female nu/nu mice, with 2 mice per time point sampling at 0.5, 2, 4, 8, 16, and 24 hours after dose, generating AUC_{0-24} for brain and plasma. To determine mouse brain $K_\mathrm{p,uu}$, the rat brain slice fu_b value that was used as brain binding is known to be species-independent (*37*). Rodent plasma fu_b values used in the $K_\mathrm{p,uu}$ calculation were determined at 1 μM to most closely match the observed in vivo levels.

To assess whether compounds were rodent efflux transporter, substrates in vivo chemical knockout studies were run. Elacridar (GF120918) at 10 mg/kg or vehicle [DMSO, 20% 2-hydroxypropyl-β-cyclodextrin (HP-β-CD) = 1:4 (v/v)] was dosed intravenously 3 hours before an oral dose (10 mg/kg) of the compound (0.5% HPMC/0.1% Tween 80) in six rats or mice. Brain and blood samples were collected at 1 hour after oral dose and used to generate K_p (brain concentration/plasma concentration) and $K_{p,uu}$ values (Eq. 4), taking an average across the six animals.

Brain/plasma ratio K_p and $K_{p,uu}$ in cynomolgus macaque monkeys

Uptake in the brain was assessed in anesthetized cynomolgus macaque using PET. The study was approved by the Animal Research Ethical Committee of the Northern Stockholm Region (N185/14) and was performed according to *Guidelines for Planning, Conducting, and Documenting Experimental Research* (Dnr 4820/06-600) of the Karolinska Institutet. The study was compliant with the AstraZeneca policies on Bioethics and Good Statistical Practice in animal work, and the EU Directive 2010/63/EU on the protection of animals used for scientific purposes. Body temperature was maintained with Bair Hugger Model 505 (Arizant Healthcare) and continuously monitored with an esophageal thermometer. Electrocardiogram, heart rate, blood pressure, respiratory rate, and oxygen saturation were continuously monitored throughout the experiments. Intravenous microdoses (<3 μg) of ^{11}C-labeled AZD1390 or AZD0156 were administered to the monkey as an intravenous bolus. Radioactivity in the brain was measured continuously for 125 min using the Siemens Molecular Imaging High Resolution Research Tomograph System. Arterial blood samples were simultaneously collected and analyzed for radioactivity in blood and plasma. The remaining parent radiolabeled compound in plasma was determined using high-performance liquid chromatography.

The delineations of anatomical brain regions were made manually on the reoriented magnetic resonance (MR) images using in-house image analysis software (*38*). Regions of interest (ROIs) for the whole brain were delineated on horizontal projection. Brain MR images were co-registered to the averaged brain PET images using SPM5 (Wellcome Department of Imaging Neuroscience). The spatially transformed ROIs were displayed on the corresponding PET images and pooled for each anatomical region. The radioactivity concentration in the brain ROI was calculated for each sequential frame, corrected for radioactive decay, and plotted versus time. The radioactivity concentration in the ROI for the whole brain was multiplied with the whole-brain ROI volume, divided by the radioactivity injected, and multiplied by 100 to obtain the percentage of radioactivity in the brain (%ID). Brain and plasma data were also expressed as the SUV corresponding to the local radioactivity concentration normalized for injected radioactivity and body weight.

Time-activity curves for [^{11}C]AZD1390 and [^{11}C]AZD0156 in the brain were corrected for radioactivity in the cerebral blood using the radioactivity concentrations in arterial blood as an estimate of the ICB blood concentration and assuming that the cerebral blood volume is 5% of the total brain volume (*39*, *40*).

Data were analyzed using kinetic 1-TC and 2-TC models (*41*, *42*). Rate constants (K_1 and k_2 in the 1-TC model, and K_1, k_2, k_3, and k_4 in the 2-TC model) were determined by curve fitting with a weighted nonlinear least-squares fitting technique. Bolus time was estimated by fitting a 2-TC model to data for the whole brain. The total volume of distribution, V_T, was subsequently calculated from the rate constants as follows.

1-TC model

$$V_T = \frac{K_1}{k_2}$$

2-TC model

$$V_T = \frac{K_1}{k_2}\left(1 + \frac{k_3}{k_4}\right)$$

The parameter V_T is equivalent to K_p and corresponds to the steady-state concentration ratio of total brain radioactivity to that in plasma. The Akaike information criterion and *F* statistics were used to determine which compartment model provided the best fit to the data. Kinetic modeling analyses were performed using PMOD version 3.6.

The unbound brain to plasma partition coefficient $K_{p,uu}$ ($C_{u,brain}$/$C_{u,plasma}$) was calculated using the following equation

$$K_{p,uu} = \frac{f_{u,brain}}{f_{u,plasma}} \times V_T$$

and values for $f_{u,brain} = 0.010$ and $f_{u,plasma} = 0.175$.

PK—Determination of drug concentration in plasma and brain

After bioluminescence of tumor tissue signals reached 10^8 to 10^9 photons/s, blood and brain tissue from individual mice were collected at 0, 1, 3, 7, 15, and 23 hours after IR dosing. AZD1390 was dosed at 1 hour before IR. Brain tissues were divided into two parts: formalin fixation for histology and pATM IHC (see below for PD analysis), and the other was snap-frozen in liquid nitrogen for PK analysis.

Blood samples were collected via cardiac puncture or retro-orbital puncture, into separate K2-EDTA–coagulated tubes, centrifuged at approximately 5000 rpm for 5 min at 2° to 8°C for plasma sampling, and stored at ~−80°C before LC-MS/MS analysis. Standards were prepared by spiking blank plasma and brain homogenate with AZD1390 covering 0.12 to 600 ng/ml (or 1.2 to 600 ng/ml). Homogenized brain tissues, along with plasma samples, were precipitated by adding fourfold volume of cold acetonitrile containing internal standard [tolbutamide (30 ng/ml)], and cerebrospinal fluid (CSF) samples were diluted with artificial CSF to 25-μl total volume and then precipitated with fourfold volume of cold acetonitrile containing internal standard. After 3-min vortex and 10-min centrifugation at 4000 rpm, the supernatant was analyzed by LC-MS/MS (API5500/QTRAP5500, Applied Biosystems). Two sets of standard curves were run at the beginning and end of each batch from blood sample analysis.

PD—ATM pathway biomarkers by IHC

Brain xenograft tissues were collected from orthotopic brain tumor–bearing mice (NCI-H2228 LC-BM model) at designated time points after IR or IR + AZD1390 treatment. Samples were formalin-fixed and paraffin-embedded (FFPE).

For γH2AX and pATM staining, 4-μm sections of FFPE tissues were used with a Lab Vision autostainer (Thermo Fisher Scientific) for IHC.

Tissue sections were dewaxed in xylene, rehydrated in graded alcohols and water, and antigen-retrieved at 110°C for 2 min (pH 9) in retrieval buffer (Dako). Sections were stained on a Lab Vision autostainer (Thermo Fisher Scientific) for 10 min and 3% hydrogen peroxide for 20 min, and serum-free protein block (Dako) was added before 60-min incubation with phospho-histone H2A.X (Ser^{139}) (CST, catalog no. 2577) or monoclonal rabbit anti-pATM (Ser^{1981}) (D25E5) antibody (CST, catalog no. 13050S) followed by 20E3 rabbit monoclonal antibody (CST) at 0.67 μg/ml in TBST (0.05%) for 30 min and EnVision+ System- HRP Labelled Polymer Anti-Rabbit (Dako) for 10 min in diaminobenzidine (DAB) (Dako). Washes were performed with TBST (0.05%). Carazzi's hematoxylin was used to counterstain the nuclei. The stained IHC slides were first reviewed and interpreted by a qualified pathologist, and then "H" scores were quantified with an Aperio system. Statistical analysis was performed using *t* test.

For pRAD50 staining, tissue sections were stained using the Ventana Discovery Ultra (Roche): 24-min EZ Prep deparaffinization at 69°C, 32-min CC1 antigen retrieval at 98°C, 32-min block with antibody diluent with casein (Roche) at 36°C, 16 min in inhibitor carboxymethyl, 32 min at 36°C in pRAD50 rabbit polyclonal antibody (#14223, CST) at 1 μg/ml in antibody diluent (Roche), 8 min at 36°C in anti-rabbit HQ (Roche), 8 min at 36°C in anti-HQ HRP (Roche), and then DAB staining (DISCOVERY ChromoMap DAB Kit). Washes were carried out in reaction buffer (Roche). Hematoxylin II and bluing reagent (Roche) were used to counterstain the nuclei. IHC-stained slides were scanned at ×20 using an Aperio AT2 scanner (Leica) and analyzed using HALO image analysis (Indica Labs). Classifiers and image analysis algorithms were developed for each biomarker using a representative training set of images. For γH2AX staining, the percentage of positive staining pixels in tumor regions was analyzed using an area quantification algorithm and tumor tissue classifier. For pRAD50 staining, a cytonuclear algorithm and tumor tissue classifier was used to quantify the percentage of nuclei with strong (3+), moderate (2+), weak (1+), or negative pRAD50 staining in tumor regions. H-score was calculated as follows: [(%1+ cells) + (%2+ cells * 2) + (%3+ cells * 3)]. One-way analysis of variance (ANOVA) with Tukey's multiple comparisons test (GraphPad Prism) was used to determine statistical differences between treatment groups for each IHC biomarker tested. A value of $P < 0.05$ was considered statistically significant.

LC-BM NCI-H2228 model development by ICB injection

Six- to 8-week-old specific pathogen–free immunodeficient nude mice were purchased from VitaRiver, and tumor models were established by injecting the human lung cancer cell line NCI-H2228 (see surgical procedure below) transfected with PLVX-luciferase-puro lentivirus to obtain luciferase stably expressing cells. A NCI-H2228-Luc stable pool cell line was selected with puromycin (2 μg/ml). Luciferase intensity was measured using the Bright-Glo Luciferase Assay System in vitro. The stability of the NCI-H2228-Luc cell line was tested before it was used for in vivo studies.

Mice were anesthetized with intraperitoneal injection with pentobarbital sodium (70 mg/kg) and their scalp was swabbed several times with alcohol-iodine, and a sagittal incision (approximately 1 cm long) was made over the parieto-occipital bone using a sterile scalpel. The skull surface was exposed using a cotton swab to make the bregma apparent, and a hole was punctured in the skull at 2.5 mm to the right of the bregma and 1 mm anterior to the coronal suture using a sterile 25-gauge sharp drill. A perpendicular syringe was placed into the skull through the hole to a depth of 3 mm below the skull surface, and H2228-Luc cell suspension was slowly injected with an infusion pump. The needle was left in place for 2 min after injection and then slowly withdrawn to check if there was any obstruction in needles. Finally, a sterile bone gel was applied to the hole, and the scalp was drawn together over the skull and stapled to close by using wound clips or silk sutures. The mice were put on heating pad softly and closely monitored daily after surgery. The bioluminescence signals were measured using an IVIS Xenogen imaging machine to monitor tumor growth.

NCI-H2228 brain metastasis model development by ICA injection

After anesthetization (as above), the mice were fixed in dorsal recumbency on heated pad and neck skin was disinfected. Then, a 1-cm mediolateral incision was made on the neck, and the trachea was exposed by blunt dissection. The muscles were separated to expose the carotid artery, which was further separated from the vagal nerve. The artery was prepared for injection distal to the point of division in the internal and external carotid arteries. The external carotid artery was temporarily occluded with an artery clamp. A ligature of 5-0 silk suture was placed around the distal part of the common carotid artery, and a second ligature was placed and tied proximal to the injection site. The artery was nicked with a pair of microscissors, and the syringe was inserted into the lumen of the blood vessel. Then, NCI-H2228-Luc cell suspension was slowly injected into the artery. After injection, the neck skin was carefully sutured. The mice were put on a heating pad softly and monitored closely every day after surgery. The bioluminescence signal was measured using an IVIS Xenogen imaging machine to monitor tumor growth.

In vivo H2228 model efficacy

Bioluminescence signaling of implanted 3×10^5 NCI-H2228-Luc cells was measured using an IVIS Xenogen imaging machine to monitor tumor growth. When the signal reached the range of 10^7 to 10^8, the mice were randomized into different treatment groups and treated orally with either vehicle or AZD1390 QD or BID + IR at 2.5 Gy daily for four consecutive days. AZD1390 or vehicle was dosed at 1 hour before IR on each dosing day. The bioluminescence signals and body weight of the mice were measured once weekly, and the raw data were recorded according to their study number and measurement date in the in vivo database. TGI from the start of treatment was assessed by comparison of the mean change in bioluminescence intensity for the control and treated groups and presented as % of TGI. The calculation of inhibition and regression was based on the geometric mean of relative tumor volume (RTV) in each group. "CG" means the geometric mean of RTV of the control group, whereas "TG" means the geometric mean of RTV of the treated group. On specific day, for each treated group, the inhibition value was calculated using the following formula: Inhibition% = (CG − TG) * 100/(CG − 1). CG should use the corresponding control group of the treated group during calculation. If inhibition was >100%, then regression was calculated using the following formula: Regression = 1 − TG. Statistical significance was evaluated using a one-tailed *t* test. Survival benefit was measured by Kaplan-Meier plots at the end of the study.

Brain tissue pathological assessment

Normal brain tissue morphology was evaluated on hematoxylin-counterstained slides using the same samples as those for PD analysis. Brain tissue morphology was evaluated in the cortical area surrounding the tumors using a scale of 0 to 3 (0, no change; 1, minimal change; 2, damage to brain cells; 3, damage and increased density of cells indicative of cell death). Damage to normal brain tissue was scored by degree of interstitial nuclear debris, spongiosis, neuronal body cell retraction, and change in the number of glial cells. Statistical analysis was carried out by one-way ANOVA followed by Bonferroni's multiple comparisons test. Notably, some samples only had $n = 1$ of valid material to score; therefore, some statistical analysis of treatments was not possible.

Establishment of syngeneic GL261-Luc cell line

The rodent glioma cell line GL261 was transfected with PLVX-luciferase-puro lentivirus. The GL261-Luc stable pool cell line was selected with puromycin (2 μg/ml) to obtain a cell line that expresses luciferase stably. The luciferase intensity was measured using the Bright-Glo Luciferase Assay System in vitro. The stability of GL261_Luc cell line was tested before it was used for in vivo studies.

Orthotopic syngeneic GL261 model development by ICB injection

Mice were anesthetized and their scalp was swabbed several times with alcohol-iodine, and a sagittal incision (approximately 1 cm long) was made over the parieto-occipital bone using a sterile scalpel. The skull surface was exposed using a cotton swab to make the bregma apparent, and a hole was punctured in the skull at 2.5 mm to the right of the bregma and 1 mm anterior to the coronal suture using a sterile 25-gauge sharp drill. A perpendicular syringe was placed into the skull through the hole to a depth of 3 mm below the skull surface, and a GL261 cell suspension was slowly injected with an infusion pump. The needle was left in place for 2 min after injection and then slowly withdrawn to check if there was any obstruction in needles. Finally, the sterile bone gel was applied to the hole, and the scalp was drawn together over the skull and stapled to close by using wound clips or silk sutures. The mice were put on heating pad softly and closely monitored daily after surgery. The bioluminescence signals were measured using an IVIS Xenogen imaging machine to monitor tumor growth.

In vivo efficacy studies in syngeneic glioma model

GL261_Luc cells (1.6×10^5) were implanted into mice through ICB injection, as described above. An IVIS Xenogen imaging machine used to monitor tumor growth measured the bioluminescence signals. When the signals reached the range of 10^7 to 10^8, the mice were randomized into treatment groups and treated orally with either vehicle, AZD1390, IR at 2.5 Gy per day for four consecutive days, IR + AZD1390, or AZD1390 + TMZ. AZD1390, TMZ, or vehicle was dosed 1 hour before IR on each dosing day. The bioluminescent signals and body weight of the mice were measured once a week. TGI from the start of treatment was assessed by comparison of the mean change in bioluminescence intensity for the control and treatment groups, and data are presented as % of TGI. The calculation of inhibition and regression was based on the geometric mean of RTV in each group. CG means the geometric mean of RTV of the control group, whereas TG means the geometric mean of RTV of the treated group. On specific day, for each treated group, inhibition value was calculated using the following formula: Inhibition% = (CG – TG) * 100/(CG – 1). CG should use the corresponding control group of the treated group during calculation. If Inhibition was >100%, then regression was calculated using the following formula: Regression = 1 – TG. Statistical significance was evaluated using a one-tailed t test. A Kaplan-Meier curve was generated to calculate the survival benefit of mice treated with compounds.

In vivo PDX efficacy studies

Human tumor tissue fragments were taken from TMZ-resistant or TMZ-sensitive GBM patients, derived from START (http://startthecure.com/preclinical_services_research.php), and implanted subcutaneously in female NMRI nude mice (Janvier Labs) between 7 and 11 weeks of age to establish the GBM PDX models. Animals were enrolled into the study when their tumor volume was approximately 200 mm^3 and randomized into four groups: vehicle, 0.5% (w/v) HPMC, and 0.1% (w/v) Tween 80 given QD for 5 days by oral gavage; 2-Gy XRT given QD for 5 days; AZD1390 (20 mg/kg) given QD for 5 days by oral gavage; and AZD1390 + XRT given QD for 5 days. XRT was performed with X-RAD 320 (Precision X-Ray) to the whole head, and AZD1390 was administered 1 hour before XRT in the combination group. Animals were observed daily, and tumor volume and body weight were measured twice per week. Tumor volumes were calculated using the following formula: 0.52 (width × length^2). All animal experiments were performed under a protocol approved by the Danish Animal Experiments Inspectorate.

SUPPLEMENTARY MATERIALS

Supplementary material for this article is available at http://advances.sciencemag.org/cgi/content/full/4/6/eaat1719/DC1
fig. S1. Mechanistic in vitro cellular activity of AZD1390.
fig. S2. Phenotypic cellular radiosensitization by AZD1390.
fig. S3. p53 status and cellular radiosensitization by AZD1390.
fig. S4. Pharmacokinetics and pharmacodynamics of AZD1390.
fig. S5. PK and PD study of single-dose AZD1390 plus IR in NCI-H2228 ICB model (ICCIN-2012).
fig. S6. In vivo activity and toxicology of AZD1390.
fig. S7. Patient-derived xenograft model characteristics.
table S1. Summary of radiosensitization of glioblastoma cells by irradiation using the colony formation assay.

REFERENCES AND NOTES

1. M. Ajaz, S. Jefferies, L. Brazil, C. Watts, A. Chalmers, Current and investigational drug strategies for glioblastoma. *Clin. Oncol. R. Coll. Radiol.* **26**, 419–430 (2014).
2. P. D. Delgado-López, E. M. Corrales-García, Survival in glioblastoma: A review on the impact of treatment modalities. *Clin. Transl. Oncol.* **18**, 1062–1071 (2016).
3. X. Lin, L. M. DeAngelis, Treatment of brain metastases. *J. Clin. Oncol.* **33**, 3475–3484 (2015).
4. G. C. M. Smith, R. B. Cary, N. D. Lakin, B. C. Hann, S.-H. Teo, D. J. Chen, S. P. Jackson, Purification and DNA binding properties of the ataxia-telangiectasia gene product ATM. *Proc. Natl. Acad. Sci. U.S.A.* **96**, 11134–11139 (1999).
5. C. J. Bakkenist, J. H. Beumer, J. C. Schmitz, ATM serine-1981 phosphorylation is a plausible biomarker. *Cell Cycle* **14**, 3207–3208 (2015).
6. C. J. Bakkenist, S. Cotterill, The 50-kDa primase subunit of *Drosophila melanogaster* DNA polymerase α. Molecular characterization of the gene and functional analysis of the overexpressed protein. *J. Biol. Chem.* **269**, 26759–26766 (1994).
7. S. Banin, L. Moyal, S.-Y. Shieh, Y. Taya, C. W. Anderson, L. Chessa, N. I. Smorodinsky, C. Prives, Y. Reiss, Y. Shiloh, Y. Ziv, Enhanced phosphorylation of p53 by ATM in response to DNA damage. *Science* **281**, 1674–1677 (1998).
8. J. Bartkova, C. J. Bakkenist, E. Rajpert-De Meyts, N. E. Skakkebæk, M. Sehested, J. Lukas, M. B. Kastan, J. Bartek, ATM activation in normal human tissues and testicular cancer. *Cell Cycle* **4**, 838–845 (2005).
9. J. Falck, N. Mailand, R. G. Syljuåsen, J. Bartek, J. Lukas, The ATM–Chk2–Cdc25A checkpoint pathway guards against radioresistant DNA synthesis. *Nature* **410**, 842–847 (2001).
10. E. C. Gosink, M. J. Chong, P. J. McKinnon, Ataxia telangiectasia mutated deficiency affects astrocyte growth but not radiosensitivity. *Cancer Res.* **59**, 5294–5298 (1999).
11. S. Matsuoka, M. Huang, S. J. Elledge, Linkage of ATM to cell cycle regulation by the Chk2 protein kinase. *Science* **282**, 1893–1897 (1998).
12. C. J. Bakkenist, M. B. Kastan, DNA damage activates ATM through intermolecular autophosphorylation and dimer dissociation. *Nature* **421**, 499–506 (2003).
13. S. T. Durant, J. A. Nickoloff, Good timing in the cell cycle for precise DNA repair by BRCA1. *Cell Cycle* **4**, 1216–1222 (2005).

14. S. T. Durant, P. Karran, Vanillins—A novel family of DNA-PK inhibitors. *Nucleic Acids Res.* **31**, 5501–5512 (2003).
15. S. T. Durant, K. S. Paffett, M. Shrivastav, G. S. Timmins, W. F. Morgan, J. A. Nickoloff, UV radiation induces delayed hyperrecombination associated with hypermutation in human cells. *Mol. Cell. Biol.* **26**, 6047–6055 (2006).
16. M. V. Bennetzen, D. H. Larsen, J. Bunkenborg, J. Bartek, J. Lukas, J. S. Andersen, Site-specific phosphorylation dynamics of the nuclear proteome during the DNA damage response. *Mol. Cell. Proteomics* **9**, 1314–1323 (2010).
17. R. Carruthers, S. U. Ahmed, K. E. Strathdee, N. Gomez-Roman, E. Amoah-Buahin, C. Watts, A. J. Chalmers, Abrogation of radioresistance in glioblastoma stem-like cells by inhibition of ATM kinase. *Mol. Oncol.* **9**, 192–203 (2015).
18. S. Choi, A. M. Gamper, J. S. White, C. J. Bakkenist, Inhibition of ATM kinase activity does not phenocopy ATM protein disruption: Implications for the clinical utility of ATM kinase inhibitors. *Cell Cycle* **9**, 4052–4057 (2010).
19. J. S. White, S. Choi, C. J. Bakkenist, Transient ATM kinase inhibition disrupts DNA damage–induced sister chromatid exchange. *Sci. Signal.* **3**, ra44 (2010).
20. S. E. Golding, E. Rosenberg, N. C. K. Valerie, I. Hussaini, M. Frigerio, X. F. Cockcroft, W. Y. Chong, M. Hummersone, L. Rigoreau, K. A. Menear, M. J. O'Connor, L. F. Povirk, T. E. van Meter, K. Valerie, Improved ATM kinase inhibitor KU-60019 radiosensitizes glioma cells, compromises insulin, AKT and ERK prosurvival signaling, and inhibits migration and invasion. *Mol. Cancer Ther.* **8**, 2894–2902 (2009).
21. L. Biddlestone-Thorpe, M. Sajjad, E. Rosenberg, J. M. Beckta, N. C. K. Valerie, M. Tokarz, B. R. Adams, A. F. Wagner, A. Khalil, D. Gilfor, S. E. Golding, S. Deb, D. G. Temesi, A. Lau, M. J. O'Connor, K. S. Choe, L. F. Parada, S. K. Lim, N. D. Mukhopadhyay, K. Valerie, ATM kinase inhibition preferentially sensitizes p53-mutant glioma to ionizing radiation. *Clin. Cancer Res.* **19**, 3189–3200 (2013).
22. Z. Guo, S. Kozlov, M. F. Lavin, M. D. Pearson, T. T. Paull, ATM activation by oxidative stress. *Science* **330**, 517–521 (2010).
23. D. Baretić, H. K. Pollard, D. I. Fisher, C. M. Johnson, B. Santhanam, C. M. Truman, T. Kouba, A. R. Fersht, C. Phillips, R. L. Williams, Structures of closed and open conformations of dimeric human ATM. *Sci. Adv.* **3**, e1700933 (2017).
24. L. Barazzuol, N. Rickett, L. Ju, P. A. Jeggo, Low levels of endogenous or X-ray-induced DNA double-strand breaks activate apoptosis in adult neural stem cells. *J. Cell Sci.* **128**, 3597–3606 (2015).
25. S. A. Gatz, L. Ju, R. Gruber, E. Hoffmann, A. M. Carr, Z.-Q. Wang, C. Liu, P. A. Jeggo, Requirement for DNA ligase IV during embryonic neuronal development. *J. Neurosci.* **31**, 10088–10100 (2011).
26. K.-H. Herzog, M. J. Chong, M. Kapsetaki, J. I. Morgan, P. J. McKinnon, Requirement for ATM in ionizing radiation-induced cell death in the developing central nervous system. *Science* **280**, 1089–1091 (1998).
27. J. C. Exell, M. J. Thompson, L. D. Finger, S. J. Shaw, J. Debreczeni, T. A. Ward, C. McWhirter, C. L. B. Siöberg, D. Martinez Molina, W. M. Abbott, C. D. Jones, J. W. M. Nissink, S. T. Durant, J. A. Grasby, Cellularly active *N*-hydroxyurea FEN1 inhibitors block substrate entry to the active site. *Nat. Chem. Biol.* **12**, 815–821 (2016).
28. M. J. O'Connor, N. M. B. Martin, G. C. M. Smith, Targeted cancer therapies based on the inhibition of DNA strand break repair. *Oncogene* **26**, 7816–7824 (2007).
29. I. Morgado-Palacin, A. Day, M. Murga, V. Lafarga, M. E. Anton, A. Tubbs, H.-T. Chen, A. V. Ergen, R. Anderson, A. Bhandoola, K. G. Pike, B. C. Barlaam, E. Cadogan, X. Wang, A. J. Pierce, C. Hubbard, S. A. Armstrong, A. Nussenzweig, O. Fernandez-Capetillo, Targeting the kinase activities of ATR and ATM exhibits antitumoral activity in mouse models of *MLL*-rearranged AML. *Sci. Signal.* **9**, ra91 (2016).
30. M. J. O'Connor, Targeting the DNA damage response in cancer. *Mol. Cell* **60**, 547–560 (2015).
31. K. G. Pike, B. Barlaam, E. Cadogan, A. Campbell, Y. Chen, N. Colclough, N. L. Davies, C. de-Almeida, S. L. Degorce, M. Didelot, A. Dishington, R. Ducray, S. T. Durant, L. A. Hassall, J. Holmes, G. D. Hughes, P. A. MacFaul, K. R. Mulholland, T. M. McGuire, G. Ouvry, M. Pass, G. Robb, N. Stratton, Z. Wang, J. Wilson, B. Zhai, K. Zhao, N. Al-Huniti, The identification of potent, selective, and orally available inhibitors of ataxia telangiectasia mutated (ATM) kinase: The discovery of AZD0156 (8-{6-[3-(dimethylamino)propoxy]pyridin-3-yl}-3-methyl-1-(tetrahydro-2*H*-pyran-4-yl)-1,3-dihydro-2*H*-imidazo[4,5-*c*]quinolin-2-one). *J. Med. Chem.* **61**, 3823–3841 (2018).
32. L. Di, H. Rong, B. Feng, Demystifying brain penetration in central nervous system drug discovery. *J. Med. Chem.* **56**, 2–12 (2013).
33. N. Beckmann, E. Giorgetti, A. Neuhaus, S. Zurbruegg, N. Accart, P. Smith, J. Perdoux, L. Perrot, M. Nash, S. Desrayaud, P. Wipfli, W. Frieauff, D. R. Shimshek, Brain region-specific enhancement of remyelination and prevention of demyelination by the CSF1R kinase inhibitor BLZ945. *Acta Neuropathol. Commun.* **6**, 9 (2018).
34. S. Banerjee, S. J. Buhrlage, H.-T. Huang, X. Deng, W. Zhou, J. Wang, R. Traynor, A. R. Prescott, D. R. Alessi, N. S. Gray, Characterization of WZ4003 and HTH-01-015 as selective inhibitors of the LKB1-tumour-suppressor-activated NUAK kinases. *Biochem. J.* **457**, 215–225 (2014).
35. J. Karlin, J. Allen, R. Odedra, G. Hughes, P. Farrington, R. Ducray, G. Ouvry, S. Degorce, J. Wilson, A. Smith, B. Patel, A. Thomason, J. Vincent, N. Colclough, S. F. Ahmad, J. M. Beckta, M. Tokarz, N. D . Mukhopadhyay, B. Barlaam, K. G. Pike, E. Cadogan, M. Pass, K. Valerie, S. Durant, Blood-brain barrier penetrating ATM inhibitor radio-sensitizes intracranial gliomas in mice, AACR 2016 (abstract #3041).
36. M. Fridén, F. Ducrozet, B. Middleton, M. Antonsson, U. Bredberg, M. Hammarlund-Udenaes, Development of a high-throughput brain slice method for studying drug distribution in the central nervous system. *Drug Metab. Dispos.* **37**, 1226–1233 (2009).
37. L. Di, J. P. Umland, G. Chang, Y. Huang, Z. Lin, D. O. Scott, M. D. Troutman, T. E. Liston, Species independence in brain tissue binding using brain homogenates. *Drug Metab. Dispos.* **39**, 1270–1277 (2011).
38. P. E. Roland, C. J. Graufelds, J. Wåhlin, L. Ingelman, M. Andersson, A. Ledberg, J. Pedersen, S. Åkerman, A. Dabringhaus, K. Zilles, Human brain atlas: For high-resolution functional and anatomical mapping. *Hum. Brain Mapp.* **1**, 173–184 (1994).
39. L. Farde, L. Eriksson, G. Blomquist, C. Halldin, Kinetic analysis of central [^{11}C]raclopride binding to D_2-dopamine receptors studied by PET—A comparison to the equilibrium analysis. *J. Cereb. Blood Flow Metab.* **9**, 696–708 (1989).
40. K. L. Leenders, D. Perani, A. A. Lammertsma, J. D. Heather, P. Buckingham, M. J. R. Healy, J. M. Gibbs, R. J. S. Wise, J. Hatazawa, S. Herold, R. P. Beaney, D. J. Brooks, T. Spinks, C. Rhodes, R. S. J. Frackowiak, T. Jones, Cerebral blood flow, blood volume and oxygen utilization. Normal values and effect of age. *Brain* **113**, 27–47 (1990).
41. M. A. Mintun, M. E. Raichle, M. R. Kilbourn, G. F. Wooten, M. J. Welch, A quantitative model for the in vivo assessment of drug binding sites with positron emission tomography. *Ann. Neurol.* **15**, 217–227 (1984).
42. S.-C. Huang, J. R. Barrio, M. E. Phelps, Neuroreceptor assay with positron emission tomography: Equilibrium versus dynamic approaches. *J. Cereb. Blood Flow Metab.* **6**, 515–521 (1986).

Acknowledgments: We are grateful to AstraZeneca Oncology IMED colleagues A. Lau, G. Smith, S. Critchlow, M. O'Connor, E. Cadogan, B. Barlaam, A. Reynolds, and W. Howatt for editorial suggestions and/or continued support for this project. We acknowledge the work by C. Nielsen and colleagues at Minerva Imaging who conducted the GBM PDX model studies and G. Hughes at AstraZeneca In Vivo Biosciences for help setting that up. We also thank AstraZeneca Early Clinical Development colleagues M. Merchant, A. Savage, G. Littlewood, and S. deVita, our lead formulation colleague D. Gore, translational scientists L. O. O'Connor and N. Lukashchuk, pharmacologists/modelers N. B. Bruna and M. Hoch, and E. Billips and A. Achanta in regulatory affairs who all lead the functions that made it possible for AZD1390 to enter phase 1 clinical trials. We are also grateful for the support provided by S. Galbraith, Head of Oncology at AstraZeneca. **Funding:** This work was predominantly funded by AstraZeneca. For the collaboration with K. Valerie, services and products in support of the research project were generated by the Virginia Commonwealth University Microscopy and Flow Cytometry Shared Resources and the Massey Cancer Center Mouse Model Core Facility, supported, in part, with funding from AstraZeneca and NIH–National Cancer Institute Cancer Center Support Grant P30CA016059, NIH R01NS064593, R21CA194789, and R21CA156995. **Author contributions:** S.T.D. leads the Bioscience of ATM projects at AstraZeneca and wrote this manuscript. L. Zheng, Y.W., K.C., L. Zhang, T.Z., and Z.Y. generated the PK, PD, and efficacy data from the orthotopic lung brain metastatic NCI-H2228 in vivo model. L.R., A.G.T., and J.H.L.F. generated in vitro target engagement and efficacy data. T.H. and K.G.P. led the chemical optimization of compounds, which led to the discovery of AZD1390. J.W., A. Smith, N.C., V.P.R., A. Sykes, A.J., P.J., K. Varnäs, and A.T. generated the PK analyses in brain tissue. S.L., J.O., J.S., C.R., and I.B. generated the in vitro potency in cell screening assays. G.J. and A.P. provided the PD analysis from the H2228 using clinically relevant translational biomarkers. M.R. provided pathological assessments in brain tissue. J.A., J. Kahn, A. Sule, J. Karlin, and K. Valerie generated the data in the murine GL261 in vivo model. A.C. and M.C. led the preclinical and clinical safety assessment. R.I. and M.P. lead and manage the AZD1390 project at AstraZeneca. **Competing interests:** T.H. and K.G.P. are inventors on a patent related to this work filed by AstraZeneca AB (No. WO 2017046216, published 23 March 2017). The following authors hold stock in AstraZeneca: S.T.D., R.I., I.B., A.S., P.J., J.W., T.H., M.P., A.C., V.P.R., M.C., G.J., A.S., J.O., A.G.T., N.C., and K.G.P. The authors declare no other competing interests. **Data and materials availability:** Data and materials will be provided by AstraZeneca pending scientific review and a completed material transfer agreement. Requests for the data and materials should be submitted to S.T.D. as point of contact.

Submitted 31 January 2018
Accepted 15 May 2018
Published 20 June 2018
10.1126/sciadv.aat1719

Citation: S. T. Durant, L. Zheng, Y. Wang, K. Chen, L. Zhang, T. Zhang, Z. Yang, L. Riches, A. G. Trinidad, J. H. L. Fok, T. Hunt, K. G. Pike, J. Wilson, A. Smith, N. Colclough, V. P. Reddy, A. Sykes, A. Janefeldt, P. Johnström, K. Varnäs, A. Takano, S. Ling, J. Orme, J. Stott, C. Roberts, I. Barrett, G. Jones, M. Roudier, A. Pierce, J. Allen, J. Kahn, A. Sule, J. Karlin, A. Cronin, M. Chapman, K. Valerie, R. Illingworth, M. Pass, The brain-penetrant clinical ATM inhibitor AZD1390 radiosensitizes and improves survival of preclinical brain tumor models. *Sci. Adv.* **4**, eaat1719 (2018).